Aquaporin-4 mediated aggregation of Alzheimer's amyloid β-peptide

Nikhil Maroli[1*]

1. Computational Biology Division, DRDO Center for Life Science, Bharathiar University Campus, Coimbatore 641046, Tamil Nadu, India

*Corresponding author: scinikhil@gmail.com

Abstract

The clearance of Alzheimer's amyloid from the brain is of utmost importance to prevent the cell toxicity. Dementia complications rise as a result of apoptosis, which is caused by the peptide's plaque at the cell's lipid surface. Here, we used all-atom and coarse-grained molecular dynamics simulation to understand how amyloid peptide aggregates at the surface of lipid and the AQP4 channel, which indirectly helps in peptide clearance from astrocytes. Through a network of protein-protein interactions, our studies showed that AQP4 and amyloid aggregation are strongly correlated. The role of aquaporin in the aetiology of Alzheimer's disease involves a number of interconnected proteins and pathways. The nature of aggregation at the surface of the POPC lipid bilayer is revealed by the interaction of the amyloid oligomers. Aquaporin, which is present in the membrane, interacts with the pore region of the channel to slow down the aggregation. The interaction keeps the peptide helical content while lowering toxicity at the lipid surface. The peptide's hydrophobicity also decreased by the interactions, which may help in the removal of the peptide from the astrocytes. Long-term coarse-grained MD simulation demonstrates different features of oligomer aggregation at the surface and strong oligomer attraction to aquaporin, which inhibits the aggregation process. Additionally, the aquaporin's water dynamics demonstrate how the selectivity filter is broken to disrupt water flow. Our findings also provide insight on the physiological alterations in brain tissue associated with Alzheimer's disease,

including water retention and increased water flow in the CSF. Further, in vitro thioflavin fluorescence spectroscopy revealed the slower aggregation of the peptide in the presence of the AQP4 channel.

Introduction

The blood-brain barrier (BBB) has an important role in the transportation and neuronal signaling of molecules. The BBB formed by the endothelial cells that line cerebral microvessels is a highly permeable 'barrier' between the circulating blood and the central nervous system. The BBB is composed of cerebral blood vessels, pericytes, perivascular microglia, perivascular neurons and astrocytes [1-2]. Astrocytes are star-shaped glial cells and their endfeet impinge on the basement membrane of the blood vessels and are highly enriched with water and potassium channels. One of the potential roles of astrocytes is balancing the potassium transport and water movement via potassium channels and aquaporin-4 channels situated in the end-feet [3-7]. Transporting therapeutic candidates across the BBB is a challenging and crucial part of any neuro/brain disease. Among those diseases, Alzheimer’s disease-one of the common forms of dementia which attracted the scientific world in the past few decades [8]. A neurodegenerative disease which starts with short-term memory loss, problems with language and gradual loss of bodily functions, leading to death [9-10]. The disease is progressive and abnormalities are first detected in the brain's frontal and temporal lobes then slowly progress to other areas of the brain depending on the individual. It is associated with the deposition of amyloid-β plaques in extracellular spaces and walls of blood vessels [11-12]. In addition to that the aggregations of the microtubules protein tau in neurofibrillary tangles cause memory loss and confusion leading to the loss of cognitive power. Amyloid-β(Aβ) peptides are the main part of the senile plaques, and several shreds of evidence support that the Aβ is a pathogenic peptide in Alzheimer’s disease which is derived from the cleavage of a larger glycoprotein-amyloid precursor protein (APP) [13-14]. APP plays

a significant role in a range of biological functions such as neuronal development, signalling and intracellular transport [15-16]. APP plays a major role in Alzheimer's disease pathogenesis, which is expressed in many tissues, especially in synapses of neurons. This precursor protein is cut by β-secretases and γ-secretases to 37 to 49 amino acid residue peptide called Aβ [17-18]. The APP is cleaved through a nonamyloidogenic pathway or amyloidogenic pathway generating α or β -C terminal fragments. Later this is further cleaved by γ-secretase and liberates the P3 and Aβ peptides, respectively. The C-terminal fragment of APP produced by β-secretase further cleaved by γ- secretase at multiple sites produces the main final form of Aβ which contains 37-49 amino acids [18]. Aβ monomer aggregates into various forms such as oligomers, protofibrils and amyloid fibrils. Amyloid fibrils are insoluble and they form plaque in the brain, whereas oligomers are soluble and distributed all over the brain [19-20]. Glenner et al. first discovered the amyloid-β from an extracellular deposit, though it's an intrinsically unstructured peptide and difficult to crystalize [21]. Later, the three-dimensional solution structure of different fragments of Aβ was determined by NMR and molecular dynamics techniques; NMR also suggested different conformation states for the $A\beta_{1-40}$ and $A\beta_{1-42}$ [22]. The residues 31-34 and 38-41 form a β-hairpin that reduces the C-terminal flexibility of $A\beta_{42}$, which is responsible for the higher tendency of $A\beta_{42}$ than $A\beta_{40}$ to form amyloid plaques [23]. Yang et al. used the replica exchange molecular dynamics method to suggest $A\beta_{40}$ and $A\beta_{42}$ can indeed populate multiple discrete conformations, including α-helix or β-sheet and they observed rapid transition in these conformations [24]. Sgourakis et al. used statistical analysis along with molecular dynamics simulation and identified a multiplicity of discrete conformational clusters in $A\beta_{42}$ [25]. Amyloid-β monomers can form higher order assemblies from low molecular weight oligomers such as dimers, trimers, tetramers, pentamers and high molecular weight oligomers like nonamers and dodecamers, to protofibrils and fibrils. Given the difficulty of obtaining high-resolution structures, alternative theoretical and simulation

approaches have been followed to rationalize the physio-chemical properties of amyloid-β and plaque formation.

Alzheimer's diseases are an imbalance between Aβ production and clearance, for an efficient strategy to cure AD it is essential to understand the clearance systems in the brain, especially transport across the blood-brain barrier. It is suggested that the astroglial-mediated interstitial fluid (ISF) bulk flow, known as the glymphatic system might be contributed in a larger portion towards the clearance of water-soluble Aβ [26-32]. Donna et al. showed that the vascular amyloid deposition with AD and CAA in both mice and human models results in the mislocalisation of aquaporin-4 expression and changes in the expression of specific potassium channels, both are essential to maintain the brain physiology [33-34]. The animal lacks aquaporin-4 in astrocytes and exhibits slow CSF influx through brain parenchyma along with perivascular spaces. Fluorescent-tagged amyloid-β was transported along this route and deletion of AQP4 genes shows the suppression of the soluble amyloid-β transportation. The expression of AQP4 in the brain of patients with or without CAA shows impaired water transport. Previous studies suggested that the expression of aquaporin-4 is high in the case of the brain affected by oedema and cerebral ischemia [35]. Further, recent studies show that AQP4 is a critical target for neuromyelitis optica [36]. The amyloid-associated proteins α1-antichuumotrypsim, apo-protein, and C1q modify amyloid-β uptake by astrocytes. The astrocytes gene expression is defective in the case of AD patients which makes further progress in AD pathology. The presence of intracellular Aβ in human astrocytes is noted by a group of researchers [29]. However, the mechanism of Aβ uptake and degradation of these cell lines are less studied. Nielsen et al. suggested that the astrocytes have the potential to bind and ingest Aβ [37]. They also shown that SCARB1 receptor plays an important role in the binding and endocytosis of Aβ in adult mouse astrocytes. Further, the expression of genes IDE, NEP and

SCARB1, MARCO LRP2 and MMP-9 associated with Aβ clearance was studied by Sandra et al. [26]. They proposed that the dysfunctional regulation of gene expression in AD astrocytes leads to the defective clearance of Aβ and promotes the accumulation of the Aβ in the brain.

Several computational studies dealt with amyloid-β aggregation and inhibition of the aggregation process via various small molecules, however, the underlying inhibitory mechanism remains elusive. Kolandaivel et al. studied the role of various metal ions, the Heme complex in the brain in action with the Aβ monomer [38]. Several reports show the inhibition of amyloid-β aggregation via analyzing the secondary structural changes of the Aβ peptide. Only a few researchers focused on the interactions of Aβ oligomers and plaque with surrounding environments. Davis et al. studied the interaction of amyloid-β with phospholipid bilayer and tetramer formation using molecular dynamic simulations [39]. They studied the $A\beta_{1-42}$ peptide interaction with zwitterion DPPC lipids and anionic DOPS phospholipid bilayers and found that the Aβ attracted towards these membrane layers and increasing the peptide-peptide interaction and leading to fast aggregation. They further provide more information about the aggregation pathway of Aβ and the putative toxic mechanism in the pathogenesis of Alzheimer's disease. Urbanc et al. studied the amyloid-β dimer formation using discrete and coarse-grained molecular dynamics simulation to estimate the thermodynamic stability of all dimer conformations [40]. The dimer conformations possess higher free energy differences than the monomer and they compare free energy between $A\beta_{1-42}$ and $A\beta_{1-40}$ dimers. Further, they found that the Aβ oligomerization is not accompanied by the formation of thermodynamically stable planer β-strand dimers. The aggregation of peptides on the lipid bilayer study using CGMD simulation in implicit solvent shows that the amyloid-β self-assemble on the surface into β-rich fibrillar aggregates even if they are dissolved in disordered oligomer form [39]. The

key interaction between the oligomerization is the Asn-Asn interaction which works like "glue" by sticking the DFNKF strands together. CGMD study of fibril-forming amphipathic peptide in the presence of lipid vesicles shows that deposition of protein aggregates on the cell membrane results in leakage and cell disruption.

Aquaporin-4 is a hetero transmembrane protein that is mostly expressed in astrocytes end foot. The blood-brain barrier is maintained and important brain activities, such as the release or uptake of neurotransmitters, are made possible by astrocytes, distinctive star-shaped glial cells found in the brain and spinal cord. We hypothesized that the interaction between amyloid-β and aquaporin-4 might be crucial for the removal of amyloid-β from the brain. Furthermore, the altered brain physiology from previous studies suggests a possible strong interaction between these proteins and peptides. To comprehend the atomic level details of amyloid-β and aquaporin, an all-atom MD simulation of amyloid-β at the surface of lipid bilayers and in the presence of AQP4 is performed. Coarse-grained molecular dynamics simulations were used to examine the interaction of oligomers and the aggregation process at the surface of lipid and lipid-protein surfaces. Additionally, thioflavin fluorescent spectroscopy was used to assess the aggregation. Finally, the protein-protein network analysis and aquaporin-4 channel water dynamics demonstrated the significant association of the amyloid peptide aggregation with the AQP4.

Result and Discussions

The structural changes of the monomer and dimer peptides in the presence of aquaporin-4 and the lipid, bilayer was analyzed using 200 ns all-atom molecular dynamics simulation. The structural features such as secondary structure, salt bridge distances, hydrogen bonds and interaction energies were calculated exclusively. The salt bridge and hydrophobicity of the peptides have a significant influence on conformational changes, aggregation, and secondary

structural changes. On the bilayer surface, lipid characteristics and conformational changes of the peptide were simulated using coarse-grained molecular dynamic simulation. In addition, thioflavin-fluorescent spectroscopy was used to assess the peptide's aggregation in vivo. Furthermore, the protein-protein interaction network reveals the hidden pathways involved in the brain's AQP4-Aβ clearance. The water dynamics of AQP4 provide insight into the brain tissue changes induced by Alzheimer's disease.

Characterization of peptide conformation at the surface of the lipid bilayer and aquaporin-4

The 42 amino acids peptide contains three important regions (Figure 1a) that are crucial in the aggregation process; central hydrophobic core region (Leu17-Ala21), loop region (Asp23-Lys28) and second hydrophobic region (Gly29-Met35) [41-44]. The native amyloid peptide monomer secondary structure consists of 78.6 % of the helix and 21.4 % coil. The residues Asp1-Ser8 adopt the bend region and Gly9-Ser26 shows the long α-helix. The interaction between His6-Gly9, Asp7-Gly9, Ala2-Arg5, and Tyr10-Gln15 residues helps to stabilize the β-hairpin structure in the region Asp1-Gln15. To elucidate the secondary structural transitions, a single peptide was simulated on the surface of the POPC lipid bilayer. During simulation, the monomer unit of amyloid-β exhibited a considerable reduction in its helical conformation; the change was gradual, and the final structure comprised 35.7% helix and 64.3% coil (Figure 2a). Figure 2(a-f) depicts the time-dependent changes to the secondary structure of the peptide in both lipid and AQP4. We placed the peptide in an aqueous environment 2.5 nm away from the surface of the lipid bilayer to avoid interactions between the peptide and lipid molecules. Simulations showed that after 200 ns, the peptide had a 35.7% helix and 64.3% coil turn in its secondary structure content. The transition from α-helix to β-sheet-rich structure is a critical part of the amyloidogenic oligomerization process. We have embedded Aquaporin-4 in the lipid membrane and kept the amyloid-β at a distance of 2.5 nm from its surface. The DSSP

calculation of the monomer secondary structure at the AQP4 surface reveals a transition from the native 78.6% helix and 21.8% coil to 76.2% helix and 23.8% coil. We observed a slower progression of the secondary structure transition when AQP4 was embedded in a lipid bilayer, as well as the retention of the peptide's helicity in the presence of AQP4. Asp1-Phe19, Lys28-Ile31, and Val39-Ala42 exhibit coil structure after 200 ns of simulation, while Phe20-Asn27 and Ile32-Gly38 exhibit helix structure at the lipid surface. In contrast, the interaction of AQP4 reveals a helix at Ala2-Gly25, Ile31-Gly38 Asp1 and coil at Ser26-Ala30. Further, the average distance between the CO^{2-} and NH^{3+} moiety of the residues was used to compute the salt-bridge distance between Asp23-Lys28 and Glu22-Lys28 (Figure 3a-c). The Asp23-Lys28 salt bridge has been implicated as having a crucial role in fibril formation. The direct salt bridge appeared at 4.3 Å, whereas the indirect or water-mediated salt bridge appeared between 4.3 Å and 7.0 Å [38]. Additionally, an indirect salt bridge of 12 Å and 11 Å were observed, indicating a weak intramolecular interaction between these residues [38]. Additionally, these interactions in the region Glu22-Lys28 preserve the turn structure throughout the simulation. When Asp23 and Lys28 are separated by a significant distance, the peptide forms a β-hairpin with a turn between residues Ala21-Val24. However, the interaction of lipids reveals a coil conformation of the peptide. In addition, the stability of the Asp23-Lys28 salt bridge was assessed by measuring the electrostatic energies between negatively charged Asp23 residues and positively charged Lys28 residues (Figure 3e-f). The simulation began with -3 kJ/mol, and up until 50 ns, a repulsive electrostatic interaction was seen between Asp23 and Lys28. With peptide at the surface, the average energy slightly increases from 0 kJ/mol to -1.5 kJ/mol. A minor repulsive interaction up to 80 ns and a gradual energy increase up to -3.5 kJ/mol were detected due to the presence of aquaporin. In addition, we assessed the salt bridge distance and electrostatic interaction energy between Glu22-Lys28 residues (Figure 3e-f). Up to 40 ns, there was absence of interaction between these residues in the peptide, and from 50 ns onwards, there is a slight

increase in energy by an average of -0.75 kJ/mol. After 80 ns, the average energy of the residues in aquaporin is 1 kJ/mol and they converge to 0.40 kJ/mol. In addition, Figure 4a-c depicts the number of hydrogen bonds formed between peptides and lipid bilayer other than the non-bonded interactions. The hydrogen bonds are estimated assuming an acceptor-hydrogen distance of less than 3 Å and a donor-hydrogen-acceptor angle of greater than 120 degrees. There was an average of four hydrogen bonds between aquaporin and monomer. Very few hydrogen bonds were found between the lipid headgroup and the peptide at 100-120 ns and 160-180 ns, with 1-2 bonds observed at each time interval. In the aquaporin-embedded system, however, there was no hydrogen bond between lipids and peptides. Furthermore, the Figure 4d-i illustrates the non-bonded interaction energies between the monomer and aquaporin and lipids. The interaction of monomers with lipids is crucial because it determines the lipids' toxicity and the conformational change of the peptide. As depicted in the Figure 4d-i, a significant amount of electrostatic interaction energy existed between the monomer and lipid surface. However, the presence of aquaporin in the membrane reduces the non-bonded interaction energy between the monomer and lipids, as expected by the hydrogen bonding analysis. Consequently, peptides exhibit strong electrostatic and van der Waals interaction energies with aquaporins in lipid membranes. The average electrostatic interaction energy is -400 kJ/mol, while the average van der Waals interaction energy is -110 kJ/mol. In addition, the distribution of the peptide monomer on the POPC lipid bilayers was observed to be more extensive than that of AQP4.

The radial distribution function of the monomer with surrounding water molecules was estimated to understand the distribution of water molecules around the peptide (Figure S1 of SI). The distribution function shows a similar pattern, but a higher shift after 0.5 nm was found in the lipid system. The distribution of water around a monomer is also influenced by the interaction of water molecules with aquaporin and the conformational transition of the peptide.

Further, in the presence of aquaporin, the hydrophobicity of monomer is found to decreases, whilst the hydrophilic area (Figure 5a-f) is stable. In the presence of aquaporin, the overall hydrophobic surface of the monomer was shown to be lower. Which is in agreement with the radial distribution function of monomers with water. Likewise, the individual residue solvent accessible surface area demonstrates higher fluctuations in the presence of aquaporin (Figure 6a-f). Also, Aquaporin reduces the number of hydrogen bonds that can form between peptides and water. The electrostatic energy between water and peptide is higher in the presence of aquaporin, whereas van der Waals interactions are lower than in a lipid-only system, indicating that the monomer units exhibit a strong interaction between lipid headgroups at the surface and a higher degree of hydrophobicity. It retains its native α-helix structure due to the presence of aquaporin in the membrane, which draws the monomer towards the pore region of the channel via strong van der Waals interactions. A recent experiment involving amyloid peptides demonstrates that the formation of toxic oligomers is a significant factor in the onset of Alzheimer's disease [45-47]. The dimer structure of a peptide on the lipid surface and the presence of aquaporin-4 were examined using all-atom MD simulations. The conformational secondary structural alterations of each monomer unit in the dimer were assessed independently. The monomer exhibits 40.5% helix, 50.0% coil, 9.5% 3-10 helix, and 52.4% helix, 47.6% coil, respectively, at the surface of the lipid bilayer (Figure 2c &d). The presence of aquaporin in the membrane, however, allowed the peptides to preserve 52.4% helix, 47.6% coil, and 74% helix, 28.2% coil, respectively (Figure 2e&f). Peptide aggregation is contingent on the interaction between individual monomer units. Indicative of the strength of monomer interactions is the number of hydrogen bonds formed between monomer units and nonbonded interactions. In the presence of aquaporin, substantially more hydrogen bonds are formed between monomer units than on the surface of lipids. In the presence of aquaporin, there are an average of five hydrogen bonds between monomers, whereas the number reduces to two at

the surface (Figure 4b&c). The figure 4b &c depicts an estimation of the number of hydrogen bonds formed between the monomers and aquaporin, hydrogen bond analysis is also consistent with the non-bonded energy. The average electrostatic interactions are -109.84 kJ/mol, however, the presence of aquaporin decreases this value to -320.78 kJ/mol. It was determined that the van der Waals interaction at the surface of lipids is -61.76 kJ/mol and -154.94 kJ/mol, respectively. In the presence of aquaporin, we have also seen the development of salt bridges between Asp23-Lys28 monomer residues.

Aggregation at the surface of lipid and aquaporin-4

The amyloid-β hypothesis implicates the ability of peptides to destabilize the cell membranes which ultimately leads to cell death [48-51]. Here, we used coarse-grained molecular dynamics simulation to understand the interactions between amyloid peptide oligomers, lipids, and aquaporin heteromers within a cell membrane. By simulating these interactions over a long period (15 µs), we can gain a better understanding of how these interactions affect the function of the cell membrane and how they may contribute to cell toxicity. The peptides were kept at a distance >2.5 nm away from the surface of the lipid bilayer to avoid any initial interactions. Figure S2-S7 of supporting information illustrates the interaction of amyloid monomers with the surface of the lipid bilayer and at the surface of the AQP4 heteromers. The simulation results demonstrate that the amyloid dimer interacts and aggregates at the surface of the lipid bilayer, in contrast to the amyloid monomer, which exhibits attraction towards AQP4 and fewer interactions with the lipid bilayer. Nonetheless, while moving from trimer to pentamer, aggregation occurs in the water and there are sporadic interactions with the lipid bilayer over the 15µs. On the contrary, the oligomers (trimer, tetrameter, and pentameter) were attracted to the AQP4 channel before aggregation in an aqueous environment. This suggests that the presence of AQP4 at the surface of the lipid bilayer hinders aggregation at the surface and results in a significant attraction towards the channel. Analyzing the deuterium order

parameter, lipid density, lipid surface area, and lipid thickness, we assessed the lipid's stability during the all-atom simulation (Figure 7a-c). On the aquaporin-embedded lipid membrane, a higher-order parameter was observed. This might be due to the presence of transmembrane protein as well as the surface interaction between monomers. Moreover, membrane thickness was shown to be almost stable in the presence of aquaporin, while simulations of the lipid-alone system revealed abrupt fluctuations in membrane thickness. Considering the simulation length of 200 ns, this demonstrates the potential toxicity of amyloid-β on lipid membranes. Variations in membrane thickness and order parameters suggest that amyloid-β produces detergent effects on the membrane. Due to the temporary and dynamic equilibrium between dimers, trimers, and tetramers, it is difficult to define the early oligomers at the atomic level using biophysical techniques. The early oligomers are the most hazardous species throughout the aggregation process. The formation of low-molecular-weight oligomers from a combination of dimers, trimers, tetramers, are characteristic of amyloid fibril forms. Several simulation studies have investigated the free energy surface and dynamics of dimers, which serve as building blocks for bigger oligomers [52-55] also the cell membrane is the primary target of amyloidogenic oligomers [56-57]. The amphipathic nature of amyloid peptides may facilitate interaction with the membrane surface and insertion into membrane cells. In addition, experimental investigations indicate that membrane interactions promote amyloid fibril formation [58-62]. We have shown, using all-atom simulations, the creation of β-structure in the dimer peptide upon interaction with lipid bilayers, although these modifications are inhibited in the presence of an aquaporin membrane. In the presence of an aquaporin channel in the membrane, the peptide-peptide interactions are drastically decreased. The interaction between the peptides disrupts the membrane structure, resulting in the dysregulation of the ion and water homeostasis [63-67]. Even though there are no particular binding sites, the interaction of the amyloidogenic peptide with the membrane surface results

in asymmetric pressure between the two lipid bilayers, uncontrolled leakage of small molecules, and a detergent-like effect [66]. Peptide aggregation is dependent on various factors, including membrane type, pH, peptides, and salt concentration [68]. The negatively charged membrane is known to produce β-strand structure, which further perturbs the membrane structure [69]. The aggregation of the peptides is also dependent on their charge and orientation; the peptide-peptide interactions rely on the orientation of the peptides in the environment, which resulted in the formation of fibrils on the surface of the membrane. As observed in the snapshot, the monomers interface with the membrane by electrostatic interactions, and the peptides align parallel to the membrane, whilst the oligomers form peptide-peptide interactions and aggregate at the membrane surface. To reveal the structural alterations, the structure of the peptide from the last frame of the CGMD was retrieved and transformed into an all-atom model. In the presence of aquaporin, the post-CG all-atom simulation reveals a higher helical content. In the presence of lipids, the secondary structure of the peptide exhibits 12.8% helix, 41.0% turn, and 46.2% coil, but in the presence of aquaporin, it shows 33.3% helix, 20.5% turn, and 46.2% coil. The 15 μs CG simulation helps to comprehend the aggregation process by changing the peptide structure over a longer period. When aquaporin is present in a membrane, the hydrogen bond between peptides and lipids is drastically weakened. However, strong hydrogen interactions occurred between peptide water molecules in both instances. In addition, the salt bridge formed between Asp23-Lys28 and Glu22-Lys28 is consistent with the first 200 ns simulation of the monomer at the membrane surface in the presence of aquaporin. On the contrary, there is no salt bridge interaction between these membrane-surface residues. This demonstrates the retention of helical content while interacting with aquaporin channels and the transformation of peptides into a more toxic β-sheet structure when interacting with the lipid bilayer.

Time-dependent aggregation of amyloid peptide-Thioflavin fluorescence spectroscopy

The *in vitro* amyloid-β aggregation was evaluated using thioflavin-based fluorescence emission. The thioflavin-T, a yellow fluorescent dye binds to the amyloid fibrils and gives intense specific emission at 490 nm. Therefore, we used this assay with varying times and concentrations of AQP4 to monitor the aquaporin-4-mediated aggregation of the amyloid peptides. Here, we have adapted an optimized procedure by Barnoli et al. to perform the assay [70]. The aggregation process of the peptide is time-dependent and aquaporin-mediated aggregation was slower than the amyloid-β alone in the same condition. Amyloid-β can adopt two different conformations in solution such as anti-parallel β-sheet and random coil or α-helix structures. The earlier one is highly amyloidogenic and the latter one is poorly amyloidogenic. The time-dependent aggregation based on fluorescent intensities are depicted in Figure 7d-f. The amyloid-β after lyophilization from HFIP solution was dissolved in DMSO. The aliquots of 2µl of amyloid-β in DMSO were incubated alone and with AQP4 with the molar ratio of 100:1 in 0.215 M sodium phosphate buffer at pH 8.0. The aggregation of the peptide occurs rapidly and intensity was measured every 15 minutes. The incubated aliquots were selected based on the 15 minutes intervals up to the lowest peak obtained (at 75 min). Several studies reported that the amyloid-β aggregates *in vitro* and forms cross-β fibrils which are similar to that found in AD patients' brains. The fluorescence intensity for both amyloid-β and amyloid-β+AQP4 was found to be reduced from 0-75 min, however, the presence of AQP4 shows slower aggregations as the intensity is found to be higher than amyloid-β alone (Figure 7 of SI). Earlier CD studies in conjunction with thioflavin spectroscopy also show the slower aggregation of the peptides in presence of AChE protein [70]. It is also observed that the presence of more AQP4 in terms of concentration was also found to be increasing intensity as a matter of slower aggregation *in vivo*. The aggregation of the peptides depends on the interaction of aquaporin channels as seen in the simulation studies is par with the experimental observations.

Water dynamics of aquaporin-4

The Figure 4d-i depicts the interaction energies, including van der Waals and electrostatic interactions, between amyloid fragments and aquaporin channels. It was revealed that the interaction energies between amyloid monomer-monomer at the lipid surface are stronger in the absence of the AQP4 channel. An average of -190 kJ/mol van der Waals and -150kJ/mol electrostatic interaction energies were found between the monomers at the surface of the lipid. However, the presence of AQP4 at the surface has shown -3 kJ/mol and -45 kJ/mol van der Waals and electrostatic interaction energy respectively. The average van der Waals and electrostatic interaction energies between monomers at the surface of the lipid were -190 kJ/mol and -150 kJ/mol, respectively. However, the presence of AQP4 at the surface has shown van der Waals and electrostatic interaction energies of -3 kJ/mol and -45 kJ/mol, respectively. This strong electrostatic interaction indicates that the channel proteins attract the amyloid fragments towards the pore region of the channel. The single monomer comprising AQP4 exhibits van der Waals and electrostatic interaction energies of -217 kJ/mol and -398 kJ/mol, respectively. In addition, it was found that the hydrogen bonds between the fragments were stronger on the surface of the lipid (2-8) than in the presence of AQP4 (1-3 hydrogen bonds). Also observed were 1-12 hydrogen bonds between amyloid monomers and the aquaporin channel. This suggests a significant affinity between amyloid peptides and AQP4. The interaction between the peptides and the water channel results in structural modifications to the pore region and the helix bundles located near the extracellular regions. The pore region of the aquaporin-4 channel is primarily controlled by the residues Arg216, Ala210, Phe77, and His201 [71]. These residues are positioned opposite one another and regulate the pore diameter for water molecule transport. To comprehend the dynamics of the pore and its associated residues, we have calculated the distance between the residues Arg216-His201 and Ala210-Phe77 (Figure 8a&b). It was revealed that the distance between residues Arg216 and His201

is shorter in the channel that interacts with the amyloid peptide monomer. In contrast, dimer interactions have the longest distance of up to 0.9 nm. It was also revealed that the distance between residues Phe77 and Ala210 is higher for both channels that interact with monomer and dimer peptides. The interaction of the peptide with the pore induces steric hindrances and structural changes in the pore. In addition to structural modifications, the interaction of peptides alters the hydrogen bonds formed between these residues and water molecules, as seen in Figure 9b&c. Peptide interactions have strengthened the formation of hydrogen bonds between Arg216, Ph77, Ala210, and His201 and the surrounding water molecules. This is owing to the huge amount of water molecules occupying the pore region, as depicted in Figure 9b&c and 10b&c. In addition, the interaction of these residues with peptides disrupted their native orientation (Figure8 h &i). The constricted pore entrance has widened, allowing more water molecules to pass through the channel. The helical structure of the AQPs is significant as it affects the structural stability of the channel and the confined size of the pore in the region of the channel containing NPA motifs. As depicted in Figure S8-S11 of SI, the time-dependent secondary structure analysis reveals stable helical structures (h1-h8). In contrast, the interaction of peptides generates infrequent coil forms and Bend and Turn formations in h7 helices. Additionally, the α-helices of the h8 region exhibit transitions to coil and bend/turn. H2 helices contain Phe77 residues, and the coil-to-turn transition found in secondary structural alterations implies the relocation of residues near the pore region (Figure8 h &i). In addition, the transition observed in small helices pushes the residues to the pore region and collapses the conventional channel cavities, resulting in the entry of several water molecules rather than a single line flow (Figure 9 b&c).

To elucidate the peptide-induced changes to the channel, the water permeation through both heteromeric and monomeric aquaporin-4 was assessed. Using a single-channel diffusive permeability constant and osmotic water permeability constant, the water permeation through

aquaporin channels was also determined. Along the +z and -z axes, Aquaporin-4 monomer units showed a total of 172 and 175 water permeation events, respectively. Under normal conditions, a single, unidirectional flow of water molecules across the aquaporin-4 and AQP2 channels as reported in the earlier studies. The interaction of amyloid peptides disrupts the channel's structure and disrupts water flow. During 200 ns, a net flow of 8396 water molecules was observed due to the monomer-AQP4 interaction, which increases the water flow across the channel. This substantially increases the water flow through the native AQP4 monomer by a factor of ten (836 water molecules). In addition to that, the dimer interaction also increases the water flow to 16372, the calculated net water flow and permeability coefficients are provided in the table 1. The interaction of the amyloid-β peptide with the pore region interrupts the single-line flow of water, and water was shown to be occupied in regions of the α-helix other than the central pore. As seen in Figure 10a, eight water molecules formed a single file in the channel. Nevertheless, the peptide-water interaction resulted in the bulk-like flow of water depicted in Figure 10b&c. This may result in the loss of the normal hydrogen bonding pattern, allowing ions or protons to possibly permeate through the channel. In addition, the estimated potential of mean force (PMF) along the direction of a single water movement revealed the conformational changes induced by the peptides. At the selectivity filter, the native AQP4 has the greatest barrier height of 4.85 kcal/mol, but the channels that interacted with single and dimer peptides have barrier heights of 1.74 kcal/mol and 0.59 kcal/mol, respectively. It is also noticed that the PMF of monomer and dimer interaction lacks a selectivity filter and that water molecules pass through the channel indiscriminately (Figure 8g). The HOLE radius displayed in the figure 10 d-f also shows a disturbance in the regular functioning of the channel and significant changes in the channel's diameter. This further implicates the physiological abnormalities of the brain reported in Alzheimer's patients related to amyloid accumulation. The brains of Alzheimer's disease patients exhibit a deterioration of normal tissue architecture

and an edematous or 'dry' characteristic. Vascular damage and reactive gliosis were also found in the majority of AD patients, accompanied by ischemic astroglial cells and APP protein [72-73]. Several experimental studies demonstrate the significance of AQP4 in the aetiology of Alzheimer's disease and the clearance of β-peptide [74-79]. However, the mechanism by which Aβ is eliminated is uncertain. As shown by the all-atom molecular dynamic's simulation, peptides cannot pass through the AQP4 channel, and earlier studies indicate that AQP4 and altered astrocyte function correlate with Alzheimer's disease, the presence of AQP4 at astrocyte cells influence the calcium and potassium homeostasis [16,80]. According to PMF calculations, the decreased height of the barrier implies the loss of normal AQP4 function: transport of water and blocking of ions, including H+, are disrupted. Larger ions, such as K+ and Ca2+, can pass through the lowered barrier and wider pores [14,16,]. The AQP4 knockout animal exhibits an increase in Aβ deposition in the cerebral cortex of 5xFAD mice; conversely, inducing the expression of the channel decreases A levels in brain tissues [81-82]. The presence of water in the CSF fluid is shown to be altered in transgenic mice with amyloid deposits due to the loss of native AQP4 function.

Protein-Protein interaction network

Analysis of the protein-protein interaction network revealed the co-occurrence of Aquaporin-4 with amyloid-. The user-specific keywords were utilized to retrieve scientific literature from PubMed databases, and our earlier approaches were modified to identify gene and protein entities mentioned in the literature. The dictionary was developed for proteins/genes with specific goals, including Aquaporin-4, amyloid-peptide, Alzheimer's disease, and Amyloid precursor protein. The biological relationship between these established co-occurring proteins and the discovered proteins/genes is depicted in the figure S12 of SI. Employing the identified proteins/genes and their relationships, Gephi 0.10 was used to construct the interaction network. In addition, several network analysis algorithms, including centrality measures, page

rank, node degree, and sub-net-node degree analysis, were applied to the network to identify the gene/protein hub and dense protein clusters. The network demonstrates that AQP4 and APP are interconnected, along with several Alzheimer's disease-related proteins (Figure S12). The extensive network diagram with all the connected proteins illustrated the numerous proteins involved in Alzheimer's disease as well as the apoptosis-related proteins such as MAPK, BCL2, CASP1, etc. The previous report revealed the co-occurrence of proteins between AQP4 and apoptosis induced by T-2 toxin-induced neuronal stress [71]. The extensive network has 1140 nodes (proteins) and 2276 edges (interactions). The network analysis leads to an identification of several proteins and linked pathways connected with AQP4-mediated amyloid peptide aggregate formation and Alzheimer's disease. In addition, we have identified 13 pathways associated with Alzheimer's disease and AQP4, including axon guidance signalling, lysosome signalling, hedgehog signalling, notch signalling, apoptosis, proteasome, MAPK signalling, pi3kakt signalling, insulin signalling, toll-like receptor signalling, pentos phosphate signalling, calcium signalling, and CAMP signalling pathways; this indicates the hidden role of Alzheimer's peptide As can be observed, the majority of pathways are involved with essential functions, however, other pathways lead to apoptosis and cell damage or oxidation, such as the involvement of MAPK pathways with AQP4 and cerebral oedema, which result in neuronal stress and cell death. MAPK pathways are also connected with numerous brain processes, such as osmolality, protein expression, and homeostasis. In addition, from the extensive network depicted in the network diagram, we have identified the key proteins related to AQP4 and Alzheimer's disease. These proteins are also recognized in a variety of biological tasks that may be linked to Alzheimer's disease and AQP4. The involvement of these pathways is either directly or indirectly related to the brain's expression of AQP4 and clearance of Aβ.

In conclusion, our studies showed a significant correlation between AQP4 and amyloid aggregation through a network of protein-protein interactions. The role of aquaporin in the

aetiology of Alzheimer's disease involves a number of interconnected proteins and pathways. The nature of aggregation at the surface of the POPC lipid bilayer is revealed by the interaction of the amyloid monomer and dimer. Aquaporin, which is present in the membrane, interacts with the pore region of the channel to slow down the aggregation. The interaction keeps the peptide helical content while lowering toxicity at the lipid surface. The peptide's hydrophobicity also reduced interactions and helped in the removal of the peptide from the astrocytes. Long-term coarse-grained MD simulation demonstrates different features of oligomer aggregation at the surface and substantial oligomer attraction to aquaporin, which inhibits the aggregation process. Additionally, the aquaporin's water dynamics demonstrate how the selectivity filter is destroyed that disrupt water flow. Our findings also provide insight on the physiological changes in brain tissue associated with Alzheimer's disease, including water retention and increased water flow in the CSF. A further demonstration of aquaporin-4's ability to minimise aggregation over time through in vitro thioflavin fluorescence spectroscopy.

Materials and methods

Protein-Membrane simulation system

The X-ray crystal structures of AQP4 [83] and Alzheimer's amyloid-peptide [84] were obtained from the PDB databank using the PDB IDs 3GD8 and 1IYT, respectively. The AQP4 tetramer was embedded in the POPC lipid bilayer after removing all co-occurring molecules, including water molecules. Prior to membrane insertion, the OPM web server [85] is utilized to align the protein to the membrane normal. The POPC membrane bilayer with 120 Å lengths in x – and y-directions were constructed using the CHARMM-GUI web server [86]. To maintain a real simulations system a water box of 30 Å thickness was added below and above the protein membrane complex and the system is neutralized with KCl ions. The single and dimer amyloid

β-peptide was placed above the lipid bilayer at a distance of 2.5 nm. The dimer peptide also kept 2.5 nm from each other and the lipid bilayer.

All-atom molecular dynamics simulation

All-atom molecular dynamics simulations of the protein-membrane system were carried out in the GROMACS 2019.6 [87-88] simulation package with the CHARMM36 forcefield [89] and TIP3P water model [90]. The particle mesh Ewald method [91] was used for the calculation of electrostatic interaction, and the Verlet cut-off scheme with a distance of 1.4 nm was used for short-range repulsive and attractive interactions. All the bonds were contained using LINCS algorithms [92] and Nose-Hoover temperature coupling along with the Parrinello-Rahman algorithm was used to maintain the temperature and pressure at 310 K and 1 bar, respectively. The simulation was performed for 200 ns at the NPT ensemble. The minimization of the system is performed using the leapfrog algorithm followed by equilibration using NVT and NPT ensemble for a total of 20 ns in six steps. The trajectories were collected every 100 ps and period boundary effects were corrected before the analysis. The water dynamics of the aquaporin channel were evaluated by calculating the number of water molecules present at the top, bottom and in the channel. The final data represented the mean of the total water molecules crossing the channel. The water permeability was calculated from the equilibrium MD simulation [93] using the following equations

$$P_d = V_w \, X \, K_0 \qquad (1)$$

$$K_0 = N\pm \, / \, (2 \, X \, n_m \, X \, t_{sim}) \qquad (2)$$

Here, V_w represents the average volume of a single water molecule and k_0 represents the number of water molecules that cross per unit of time. Nm, represents the number of monomer units and t_{sim} is the total duration of the simulation. Further, the permeability coefficient (pf) calculated from the collective diffusion constant, defined according to the Einstein relation as;

$$D_n = \langle n_{2(t)}/2t \rangle \quad (3)$$

Where <n2(t)/2t> is the mean square displacement of n(t), the osmotic permeability constant (pf) calculated as

$$P_f - V_w \text{ X } D_n \quad (4)$$

Steered molecular dynamics and umbrella sampling

The free energy of transportation of water molecules through the aquaporin channel has been obtained by constructing the PMF (potential of mean force). The PMF profiles provide the energy required for a water molecule from one end of the channel to the other end. Here we have extracted the last frame of AQP4 at 200 ns all-atom simulation for the steered molecular dynamics simulation. The PMF is calculated for the apo state of AQP4 and the channel that interreacted with single and dimer amyloid-β peptide. The water molecules are placed ~5 Å away from the pore of the channel and pulled through the channel cavity. The simulation box is maintained to satisfy the minimum image convention and provide sufficient space for pulling along the z-axis. The system was equilibrated with an NPT ensemble for the short period of 1 ns and minimized for 5000 steps. The temperature and pressure were maintained at 310 K and 1 bar using Berendsen weak coupling method. The pulling simulations (SMD) are performed by keeping the channel as a reference group with a harmonic spring constant of 900 kJmol-1nm-2 with a pulling rate of 0.001 nmps-1. The histograms are generated with a window spacing of 0.2 nm and approximately 450 frames corresponding to the COM distance between the reference and pulling group. Each window was used to perform a 10 ns umbrella sampling simulation and the PMF profile was constructed for each molecule which provides the ΔG value for the transportation of water molecules. The weighted histogram analysis method (WHAM) was used to estimate the free energy profile from the umbrella simulations [94].

Coarse-Grained molecular dynamics simulation

The lipid bilayer of 120 x 120 Å, Aquaporin-4 embedded lipid bilayer with amyloid-β was constructed with Martini builder with the help of the CHARMM-GUI web server. In the martini model, heavy atoms like C, N, and O and their associated hydrogen atoms are considered single beads. The simulation of 15 μs was performed with GROMACS using standard martini v2.2 forcefield [95-96] for proteins, lipids, water and ions. The steepest decent algorithm was used to minimize the neutralized system and equilibration was achieved with multiple steps by adapting the step-wise releasing of restrains applied on lipids. The periodic boundary conditions were applied and a time step of 30 fs was used electrostatic interaction was truncated with a shift cutoff of 1.2 nm and Lennard-Jones (LJ) potential was smoothly shifted to zero within 0.9 to 1.2 nm during the simulations. The temperature and pressure were maintained at 310 K and 1 bar using Berendsen and the velocity-rescaling method. The trajectories were saved at every 20 fs and all the visualization was performed with VMD software packages [97].

Protein-Protein network analysis

The protein-protein interaction network is constructed to understand the associated protein between the AQP4 and amyloid β-peptide including Alzheimer's disease. Here, we have used our previous method [98,74], which uses the harvesting of entries from PubMed using suitable keywords. The keywords such as "AQP4" and "aquaporin-4" returned a total of 4820 documents and amyloid β-peptide including Alzheimer's disease returned 415,321 entries, respectively. The extracted data were used to construct the relation network using the visual ion tool Gephi 0.10 [99]. Several network analysis algorithms and parameters such as centrality measures, page rank, node degree, graph density and sub-net-work analysis were performed on the network. The centrality measures provide the highly dense or most important highly connected nodes in the network. PageRank algorithm prides the relative importance of a particular node in the network based on its network connectivity. Further, we have reduced the

broad network obtained from the above keywords into the small network where the most important proteins were identified.

Thioflavin T-based fluorometric assay

Thioflavin T, amyloid-β peptide, DMSO, HFIP and other reagents were from Sigma Aldrich. The aquaporin-4 and amyloid-β antibodies and proteins were from Elabscience. The stock solution of $A\beta_{1-42}$ with a concentration of 2 mg/ml was prepared by suspending 1 mg of $A\beta_{1-42}$ with 0.5 mL of 1,1,1,3,3,3-hexafluoro-2-propanol (HFIP). The rapid aggregation of $A\beta_{1-42}$ was prevented by water batch sonication for 10 min. The aliquots of the peptide were stored at -80 °C and freshly thawed samples were used for the analysis. The thawed samples were sonicated for 5 min or till the evaporation of the HFIP. Further, the sodium hydroxide solution was used to titrate the solution to a pH range of 8-9. For co-incubation experiments, a buffer solution of peptide and aquaporin was added in a molar ratio of (AQP4: $A\beta_{1-42}$) 100:1 to perform a thioflavin T fluorescence experiment and an incubation experiment was performed for some time of 0-72 hrs. The thioflavin T-based fluorometric assay was performed with Horiba Jobin–Yvon Fluromax 4 using a 3 mL quartz cell. Fluorescence was monitored at 446 nm and 490 nm with excitation and emission slits of 2 nm bandwidth. The fluorescence emission spectrum was recorded between 450 and 600 nm, with excitation at 446 nm. The sample was analyzed after incubation, and the solution containing $A\beta_{1-42}$, $A\beta_{1-42}$ with aquaporin-4 was added to 50 mM glycine-NaOH buffer (pH 8.5) containing 1.5 μM thioflavin T in a final volume of 2 ml. A time scan of fluorescent was performed and the intensity values reached the plateau were average after subtracting the background fluorescent from thioflavin T and AQP4.

Associated content

Supporting Information

Acknowledgements

Author thank Prof P Kolandaivel for useful discussions and support.

References

(1) Scheltens, P.; Blennow, K.; Breteler, M. M. B.; de Strooper, B.; Frisoni, G. B.; Salloway, S.; Van der Flier, W. M. Alzheimer's Disease. *Lancet* **2016**, *388* (10043), 505–517. https://doi.org/10.1016/S0140-6736(15)01124-1.

(2) Zhou, B.; Zuo, Y. X.; Jiang, R. T. Astrocyte Morphology: Diversity, Plasticity, and Role in Neurological Diseases. *CNS Neurosci. Ther.* **2019**, *25* (6), 665–673. https://doi.org/10.1111/cns.13123.

(3) Gunnarson, E.; Axehult, G.; Baturina, G.; Zelenin, S.; Zelenina, M.; Aperia, A. Lead Induces Increased Water Permeability in Astrocytes Expressing Aquaporin 4. *Neuroscience* **2005**, *136* (1), 105–114. https://doi.org/10.1016/j.neuroscience.2005.07.027.

(4) Abbott, N. J.; Patabendige, A. A. K.; Dolman, D. E. M.; Yusof, S. R.; Begley, D. J. Structure and Function of the Blood-Brain Barrier. *Neurobiol. Dis.* **2010**, *37* (1), 13–25. https://doi.org/10.1016/j.nbd.2009.07.030.

(5) Hubbard, J. A.; Hsu, M. S.; Seldin, M. M.; Binder, D. K. Expression of the Astrocyte Water Channel Aquaporin-4 in the Mouse Brain. *ASN Neuro* **2015**, *7* (5). https://doi.org/10.1177/1759091415605486.

(6) Pauwels, K.; Williams, T. L.; Morris, K. L.; Jonckheere, W.; Vandersteen, A.; Kelly, G.; Schymkowitz, J.; Rousseau, F.; Pastore, A.; Serpell, L. C.; Broersen, K. Structural Basis for Increased Toxicity of Pathological Aβ42:Aβ40 Ratios in Alzheimer Disease. *J. Biol. Chem.* **2012**, *287* (8), 5650–5660. https://doi.org/10.1074/jbc.M111.264473.

(7) Dobbing, J. The Blood-Brain Barrier. *Dev. Med. Child Neurol.* **1961**, *3* (6), 610–612. https://doi.org/10.1111/j.1469-8749.1961.tb10430.x.

(8) Chow, V. W.; Mattson, M. P.; Wong, P. C.; Gleichmann, M. An Overview of APP Processing Enzymes and Products. *Neuromolecular Med.* **2010**, *12* (1), 1–12. https://doi.org/10.1007/s12017-009-8104-z.

(9) Ballard, C.; Gauthier, S.; Corbett, A.; Brayne, C.; Aarsland, D.; Jones, E. Alzheimer's Disease. *Lancet* **2011**, *377* (9770), 1019–1031. https://doi.org/10.1016/S0140-6736(10)61349-9.

(10) Haass, C.; Selkoe, D. J. Cellular Processing of P-Amyloid Precursor Protein and the Genesis of Amyloid P-Peptide Minireview. *Cell* **1993**, *75*, 1039–1042.

(11) Smith, D. G.; Cappai, R.; Barnham, K. J. The Redox Chemistry of the Alzheimer's Disease Amyloid β Peptide. *Biochim. Biophys. Acta - Biomembr.* **2007**, *1768* (8), 1976–1990. https://doi.org/10.1016/j.bbamem.2007.02.002.

(12) Camassa, L. M. A.; Lunde, L. K.; Hoddevik, E. H.; Stensland, M.; Boldt, H. B.; De Souza, G. A.; Ottersen, O. P.; Amiry-Moghaddam, M. Mechanisms Underlying AQP4 Accumulation in Astrocyte Endfeet. *Glia* **2015**, *63* (11), 2073–2091. https://doi.org/10.1002/glia.22878.

(13) Abbott, N. J. Astrocyte-Endothelial Interactions and Blood-Brain Barrier Permeability. *J. Anat.* **2002**, *200* (6), 629–638. https://doi.org/10.1046/j.1469-7580.2002.00064.x.

(14) Carter, S. F.; Herholz, K.; Rosa-Neto, P.; Pellerin, L.; Nordberg, A.; Zimmer, E. R. Astrocyte Biomarkers in Alzheimer's Disease. *Trends Mol. Med.* **2019**, *25* (2), 77–95. https://doi.org/10.1016/j.molmed.2018.11.006.

(15) Hartmann, T. Intracellular Biology of Alzheimer's Disease Amyloid Beta Peptide. *Eur. Arch. Psychiatry Clin. Neurosci.* **1999**, *249* (6), 291–298. https://doi.org/10.1007/s004060050102.

(16) Fong, L. K.; Yang, M. M.; Chaves, R. dos S.; Reyna, S. M.; Langness, V. F.; Woodruff, G.; Roberts, E. A.; Young, J. E.; Goldstein, L. S. B. Full-Length Amyloid Precursor Protein Regulates Lipoprotein Metabolism and Amyloid- Clearance in Human Astrocytes. *J. Biol. Chem.* **2018**, *293* (29), 11341–11357. https://doi.org/10.1074/jbc.RA117.000441.

(17) Ferreira, S. T.; Klein, W. L. The Aβ Oligomer Hypothesis for Synapse Failure and Memory Loss in Alzheimer's Disease. *Neurobiol. Learn. Mem.* **2011**, *96* (4), 529–543. https://doi.org/10.1016/j.nlm.2011.08.003.

(18) Verkhratsky, A.; Olabarria, M.; Noristani, H. N.; Yeh, C.; Rodriguez, J. J. <10.1016-J.Nurt.2010.05.017.Pdf>. **2010**, *7* (October), 399–412.

(19) Bolduc, D. M.; Montagna, D. R.; Seghers, M. C.; Wolfe, M. S.; Selkoe, D. J. The Amyloid-Beta Forming Tripeptide Cleavage Mechanism of γ-Secretase. *Elife* **2016**, *5* (AUGUST), 1–21. https://doi.org/10.7554/eLife.17578.

(20) Demuro, A.; Parker, I.; Stutzmann, G. E. Calcium Signaling and Amyloid Toxicity in Alzheimer Disease. *J. Biol. Chem.* **2010**, *285* (17), 12463–12468. https://doi.org/10.1074/jbc.R109.080895.

(21) Crescenzi, O.; Tomaselli, S.; Guerrini, R.; Salvadori, S.; D'Ursi, A. M.; Temussi, P. A.; Picone, D. Solution Structure of the Alzheimer Amyloid β-Peptide (1-42) in an Apolar Microenvironment: Similarity with a Virus Fusion Domain. *Eur. J. Biochem.* **2002**, *269* (22), 5642–5648. https://doi.org/10.1046/j.1432-1033.2002.03271.x.

(22) D Isaacson, J L Mueller, J. C. N. and S. S.; Article, R. 基因的改变NIH Public Access. *Bone* **2006**, *23* (1), 1–7. https://doi.org/10.1007/978-3-540-79885-9.

(23) He, X. F.; Liu, D. X.; Zhang, Q.; Liang, F. Y.; Dai, G. Y.; Zeng, J. S.; Pei, Z.; Xu, G. Q.; Lan, Y. Voluntary Exercise Promotes Glymphatic Clearance of Amyloid Beta and Reduces the Activation of Astrocytes and Microglia in Aged Mice. *Front. Mol. Neurosci.* **2017**, *10* (May), 1–14. https://doi.org/10.3389/fnmol.2017.00144.

(24) Chen, G. F.; Xu, T. H.; Yan, Y.; Zhou, Y. R.; Jiang, Y.; Melcher, K.; Xu, H. E. Amyloid Beta: Structure, Biology and Structure-Based Therapeutic Development. *Acta Pharmacol. Sin.* **2017**, *38* (9), 1205–1235. https://doi.org/10.1038/aps.2017.28.

(25) Mulder, S. D.; Veerhuis, R.; Blankenstein, M. A.; Nielsen, H. M. The Effect of Amyloid Associated Proteins on the Expression of Genes Involved in Amyloid-β Clearance by Adult Human Astrocytes. *Exp. Neurol.* **2012**, *233* (1), 373–379. https://doi.org/10.1016/j.expneurol.2011.11.001.

(26) Glenner, G. G.; Wong, C. W. Alzheimer's Disease: Initial Report of the Purification and Characterization of a Novel Cerebrovascular Amyloid Protein. *Biochem. Biophys. Res. Commun.* **1984**, *120* (3), 885–890. https://doi.org/10.1016/S0006-291X(84)80190-4.

(27) Sgourakis, N. G.; Merced-serrano, M.; Boutsidis, C.; Du, Z.; Wang, C.; Garcia, A. E. Simulations and Spectral Algorithms. **2012**, *405* (2), 570–583. https://doi.org/10.1016/j.jmb.2010.10.015.Atomic-level.

(28) Yip, C. M.; Darabie, A. A.; McLaurin, J. A. Aβ42-Peptide Assembly on Lipid Bilayers. *J. Mol. Biol.* **2002**, *318* (1), 97–107. https://doi.org/10.1016/S0022-2836(02)00028-1.

(29) Yang, M.; Teplow, D. B. Amyloid β-Protein Monomer Folding: Free-Energy Surfaces Reveal Alloform-Specific Differences. *J. Mol. Biol.* **2008**, *384* (2), 450–464. https://doi.org/10.1016/j.jmb.2008.09.039.

(30) Thal, D. R. The Role of Astrocytes in Amyloid β-Protein Toxicity and Clearance. *Exp. Neurol.* **2012**, *236* (1), 1–5. https://doi.org/10.1016/j.expneurol.2012.04.021.

(31) Wilcock, D. M.; Rojiani, A.; Rosenthal, A.; Subbarao, S.; Freeman, M. J.; Gordon, M. N.; Morgan, D. Passive Immunotherapy against Aβ in Aged APP-Transgenic Mice Reverses Cognitive Deficits and Depletes Parenchymal Amyloid Deposits in Spite of Increased Vascular Amyloid and Microhemorrhage. *J. Neuroinflammation* **2004**, *1*, 1–11. https://doi.org/10.1186/1742-2094-1-24.

(32) Wilcock, D. M.; Vitek, M. P.; Colton, C. A. Vascular Amyloid Alters Astrocytic Water and Potassium Channels in Mouse Models and Humans with Alzheimer's Disease. *Neuroscience* **2009**, *159* (3), 1055–1069. https://doi.org/10.1016/j.neuroscience.2009.01.023.

(33) D Isaacson, J L Mueller, J. C. N. and S. S.; Article, R. 基因的改变NIH Public Access. *Bone* **2006**, *23* (1), 1–7. https://doi.org/10.1007/978-3-540-79885-9.

(34) Prasad, H.; Rao, R. Amyloid Clearance Defect in ApoE4 Astrocytes Is Reversed by Epigenetic Correction of Endosomal PH. *Proc. Natl. Acad. Sci. U. S. A.* **2018**, *115* (28), E6640–E6649. https://doi.org/10.1073/pnas.1801612115.

(35) Palazzo, C.; Buccoliero, C.; Mola, M. G.; Abbrescia, P.; Nicchia, G. P.; Trojano, M.; Frigeri, A. AQP4ex Is Crucial for the Anchoring of AQP4 at the Astrocyte End-Feet and Fo Neuromyelitis Optica Antibody Binding. *Acta Neuropathol. Commun.* **2019**, *7* (1), 1–15. https://doi.org/10.1186/s40478-019-0707-5.

(36) Liu, C. C.; Hu, J.; Zhao, N.; Wang, J.; Wang, N.; Cirrito, J. R.; Kanekiyo, T.; Holtzman, D. M.; Bu, G. Astrocytic LRP1 Mediates Brain Aβ Clearance and Impacts

Amyloid Deposition. *J. Neurosci.* **2017**, *37* (15), 4023–4031. https://doi.org/10.1523/JNEUROSCI.3442-16.2017.

(37) Boopathi, S.; Kolandaivel, P. Role of Zinc and Copper Metal Ions in Amyloid β-Peptides Aβ1-40 and Aβ1-42 Aggregation. *RSC Adv.* **2014**, *4* (73), 38951–38965. https://doi.org/10.1039/c4ra05390g.

(38) Brown, A. M.; Bevan, D. R. Molecular Dynamics Simulations of Amyloid β-Peptide (1-42): Tetramer Formation and Membrane Interactions. *Biophys. J.* **2016**, *111* (5), 937–949. https://doi.org/10.1016/j.bpj.2016.08.001.

(39) Nielsen, H. M.; Veerhuis, R.; Holmqvist, B.; Janciauskiene, S. Binding and Uptake of Aβ1-42 by Primary Human Astrocytes in Vitro. *Glia* **2009**, *57* (9), 978–988. https://doi.org/10.1002/glia.20822.

(40) Urbanc, B.; Cruz, L.; Ding, F.; Sammond, D.; Khare, S.; Buldyrev, S. V.; Stanley, H. E.; Dokholyan, N. V. Molecular Dynamics Simulation of Amyloid β Dimer Formation. *Biophys. J.* **2004**, *87* (4), 2310–2321. https://doi.org/10.1529/biophysj.104.040980.

(41) Tarus, B.; Straub, J. E.; Thirumalai, D. Dynamics of Asp23-Lys28 Salt-Bridge Formation in Aβ10-35 Monomers. *J. Am. Chem. Soc.* **2006**, *128* (50), 16159–16168. https://doi.org/10.1021/ja064872y.

(42) Walsh, D. M.; Klyubin, I.; Fadeeva, J. V.; Cullen, W. K.; Anwyl, R.; Wolfe, M. S.; Rowan, M. J.; Selkoe, D. J. Naturally Secreted Oligomers of Amyloid β Protein Potently Inhibit Hippocampal Long-Term Potentiation in Vivo. *Nature* **2002**, *416* (6880), 535–539. https://doi.org/10.1038/416535a.

(43) Ono, K.; Condron, M. M.; Teplow, D. B. Effects of the English (H6R) and Tottori (D7N) Familial Alzheimer Disease Mutations on Amyloid β-Protein Assembly and Toxicity. *J. Biol. Chem.* **2010**, *285* (30), 23186–23197. https://doi.org/10.1074/jbc.M109.086496.

(44) Gurlo, T.; Ryazantsev, S.; Huang, C. J.; Yeh, M. W.; Reber, H. A.; Hines, O. J.; O'Brien, T. D.; Glabe, C. G.; Butler, P. C. Evidence for Proteotoxicity in β Cells in Type 2 Diabetes: Toxic Islet Amyloid Polypeptide Oligomers Form Intracellularly in the Secretory Pathway. *Am. J. Pathol.* **2010**, *176* (2), 861–869. https://doi.org/10.2353/ajpath.2010.090532.

(45) Bokvist, M.; Lindström, F.; Watts, A.; Gröbner, G. Two Types of Alzheimer's β-Amyloid (1-40) Peptide Membrane Interactions: Aggregation Preventing Transmembrane Anchoring Versus Accelerated Surface Fibril Formation. *J. Mol. Biol.* **2004**, *335* (4), 1039–1049. https://doi.org/10.1016/j.jmb.2003.11.046.

(46) Berhanu, W. M.; Hansmann, U. H. E. Structure and Dynamics of Amyloid-β Segmental Polymorphisms. *PLoS One* **2012**, *7* (7). https://doi.org/10.1371/journal.pone.0041479.

(47) Jang, H.; Connelly, L.; Arce, F. T.; Ramachandran, S.; Lal, R.; Kagan, B. L.; Nussinov, R. Alzheimer's Disease: Which Type of Amyloid-Preventing Drug Agents

to Employ? *Phys. Chem. Chem. Phys.* **2013**, *15* (23), 8868–8877. https://doi.org/10.1039/c3cp00017f.

(48) Kremer, J. J.; Pallitto, M. M.; Sklansky, D. J.; Murphy, R. M. Correlation of β-Amyloid Aggregate Size and Hydrophobicity with Decreased Bilayer Fluidity of Model Membranes. *Biochemistry* **2000**, *39* (33), 10309–10318. https://doi.org/10.1021/bi0001980.

(49) Petkova, A. T.; Leapman, R. D.; Guo, Z.; Yau, W. M.; Mattson, M. P.; Tycko, R. Self-Propagating, Molecular-Level Polymorphism in Alzheimer's β-Amyloid Fibrils. *Science (80-.).* **2005**, *307* (5707), 262–265. https://doi.org/10.1126/science.1105850.

(50) Mingeot-Leclercq, M. P.; Lins, L.; Bensliman, M.; Van Bambeke, F.; Van Der Smissen, P.; Peuvot, J.; Schanck, A.; Brasseur, R. Membrane Destabilization Induced by β-Amyloid Peptide 29-42: Importance of the Amino-Terminus. *Chem. Phys. Lipids* **2002**, *120* (1–2), 57–74. https://doi.org/10.1016/S0009-3084(02)00108-1.

(51) Jayasinghe, S. A.; Langen, R. Lipid Membranes Modulate the Structure of Islet Amyloid Polypeptide. *Biochemistry* **2005**, *44* (36), 12113–12119. https://doi.org/10.1021/bi050840w.

(52) Butterfield, S. M.; Lashuel, H. A. Amyloidogenic Protein-Membrane Interactions: Mechanistic Insight from Model Systems. *Angew. Chemie - Int. Ed.* **2010**, *49* (33), 5628–5654. https://doi.org/10.1002/anie.200906670.

(53) Quist, A.; Doudevski, I.; Lin, H.; Azimova, R.; Ng, D.; Frangione, B.; Kagan, B.; Ghiso, J.; Lal, R. Amyloid Ion Channels: A Common Structural Link for Protein-Misfolding Disease. *Proc. Natl. Acad. Sci. U. S. A.* **2005**, *102* (30), 10427–10432. https://doi.org/10.1073/pnas.0502066102.

(54) Coates, D. R.; Chin, J. M.; Chung, S. T. L. 基因的改变NIH Public Access. *Bone* **2011**, *23* (1), 1–7. https://doi.org/10.1021/ct300916f.Mechanisms.

(55) Walsh, D. M.; Klyubin, I.; Fadeeva, J. V.; Cullen, W. K.; Anwyl, R.; Wolfe, M. S.; Rowan, M. J.; Selkoe, D. J. Naturally Secreted Oligomers of Amyloid β Protein Potently Inhibit Hippocampal Long-Term Potentiation in Vivo. *Nature* **2002**, *416* (6880), 535–539. https://doi.org/10.1038/416535a.

(56) LIN, H.; BHATIA, R.; LAL, R. Amyloid β Protein Forms Ion Channels: Implications for Alzheimer's Disease Pathophysiology. *FASEB J.* **2001**, *15* (13), 2433–2444. https://doi.org/10.1096/fj.01-0377com.

(57) Gurlo, T.; Ryazantsev, S.; Huang, C. J.; Yeh, M. W.; Reber, H. A.; Hines, O. J.; O'Brien, T. D.; Glabe, C. G.; Butler, P. C. Evidence for Proteotoxicity in β Cells in Type 2 Diabetes: Toxic Islet Amyloid Polypeptide Oligomers Form Intracellularly in the Secretory Pathway. *Am. J. Pathol.* **2010**, *176* (2), 861–869. https://doi.org/10.2353/ajpath.2010.090532.

(58) Bokvist, M.; Lindström, F.; Watts, A.; Gröbner, G. Two Types of Alzheimer's β-Amyloid (1-40) Peptide Membrane Interactions: Aggregation Preventing Transmembrane Anchoring Versus Accelerated Surface Fibril Formation. *J. Mol. Biol.* **2004**, *335* (4), 1039–1049. https://doi.org/10.1016/j.jmb.2003.11.046.

(59) Jang, H.; Connelly, L.; Arce, F. T.; Ramachandran, S.; Lal, R.; Kagan, B. L.; Nussinov, R. Alzheimer's Disease: Which Type of Amyloid-Preventing Drug Agents to Employ? *Phys. Chem. Chem. Phys.* **2013**, *15* (23), 8868–8877. https://doi.org/10.1039/c3cp00017f.

(60) Murphy, M. P.; Levine, H. Alzheimer's Disease and the Amyloid-β Peptide. *J. Alzheimer's Dis.* **2010**, *19* (1), 311–323. https://doi.org/10.3233/JAD-2010-1221.

(61) Knight, J. D.; Miranker, A. D. Phospholipid Catalysis of Diabetic Amyloid Assembly. *J. Mol. Biol.* **2004**, *341* (5), 1175–1187. https://doi.org/10.1016/j.jmb.2004.06.086.

(62) Sparr, E.; Engel, M. F. M.; Sakharov, D. V.; Sprong, M.; Jacobs, J.; De Kruijff, B.; Höppener, J. W. M.; Antoinette Killian, J. Islet Amyloid Polypeptide-Induced Membrane Leakage Involves Uptake of Lipids by Forming Amyloid Fibers. *FEBS Lett.* **2004**, *577* (1–2), 117–120. https://doi.org/10.1016/j.febslet.2004.09.075.

(63) Terzi, E.; Hölzemann, G.; Seelig, J. Self-Association of β-Amyloid Peptide (1-40) in Solution and Binding to Lipid Membranes. *J. Mol. Biol.* **1995**, *252* (5), 633–642. https://doi.org/10.1006/jmbi.1995.0525.

(64) Williams, T. L.; Serpell, L. C. Membrane and Surface Interactions of Alzheimer's Aβ Peptide - Insights into the Mechanism of Cytotoxicity. *FEBS J.* **2011**, *278* (20), 3905–3917. https://doi.org/10.1111/j.1742-4658.2011.08228.x.

(65) Mirzabekov, T. A.; Lin, M. C.; Kagan, B. L. Pore Formation by the Cytotoxic Islet Amyloid Peptide Amylin. *J. Biol. Chem.* **1996**, *271* (4), 1988–1992. https://doi.org/10.1074/jbc.271.4.1988.

(66) Hardy, J. A.; Higgins, G. A. Alzheimer's Disease: The Amyloid Alzheimer's Disease. *Science (80-.).* **1992**, *256* (5054), 184–185.

(67) Bartolini, M.; Bertucci, C.; Cavrini, V.; Andrisano, V. β-Amyloid Aggregation Induced by Human Acetylcholinesterase: Inhibition Studies. *Biochem. Pharmacol.* **2003**, *65* (3), 407–416. https://doi.org/10.1016/S0006-2952(02)01514-9.

(68) Sokolov, Y.; Kozak, J. A.; Kayed, R.; Chanturiya, A.; Glabe, C.; Hall, J. E. Soluble Amyloid Oligomers Increase Bilayer Conductance by Altering Dielectric Structure. *J. Gen. Physiol.* **2006**, *128* (6), 637–647. https://doi.org/10.1085/jgp.200609533.

(69) McLaurin, J. A.; Chakrabartty, A. Characterization of the Interactions of Alzheimer β-Amyloid Peptides with Phospholipid Membranes. *Eur. J. Biochem.* **1997**, *245* (2), 355–363. https://doi.org/10.1111/j.1432-1033.1997.t01-2-00355.x.

(70) Knight, J. D.; Hebda, J. A.; Miranker, A. D. Conserved and Cooperative Assembly of Membrane-Bound α-Helical States of Islet Amyloid Polypeptide. *Biochemistry* **2006**, *45* (31), 9496–9508. https://doi.org/10.1021/bi060579z.

(71) Zeppenfeld, D. M.; Simon, M.; Haswell, J. D.; D'Abreo, D.; Murchison, C.; Quinn, J. F.; Grafe, M. R.; Woltjer, R. L.; Kaye, J.; Iliff, J. J. Association of Perivascular Localization of Aquaporin-4 with Cognition and Alzheimer Disease in Aging Brains. *JAMA Neurol.* **2017**, *74* (1), 91–99. https://doi.org/10.1001/jamaneurol.2016.4370.

(72) Chun, H.; Marriott, I.; Lee, C. J.; Cho, H. Elucidating the Interactive Roles of Glia in Alzheimer's Disease Using Established and Newly Developed Experimental Models. *Front. Neurol.* **2018**, *9* (SEP), 1–11. https://doi.org/10.3389/fneur.2018.00797.

(73) Liu, C. Y.; Yang, Y.; Ju, W. N.; Wang, X.; Zhang, H. L. Emerging Roles of Astrocytes in Neuro-Vascular Unit and the Tripartite Synapse with Emphasis on Reactive Gliosis in the Context of Alzheimer's Disease. *Front. Cell. Neurosci.* **2018**, *12* (July), 1–12. https://doi.org/10.3389/fncel.2018.00193.

(74) Maroli, N.; Kalagatur, N. K.; Bhasuran, B.; Jayakrishnan, A.; Manoharan, R. R.; Kolandaivel, P.; Natarajan, J.; Kadirvelu, K. Molecular Mechanism of T-2 Toxin-Induced Cerebral Edema by Aquaporin-4 Blocking and Permeation. *J. Chem. Inf. Model.* **2019**, *59* (11), 4942–4958. https://doi.org/10.1021/acs.jcim.9b00711.

(75) Oh, S. J.; Lee, H. J.; Kang, K. J.; Han, S. J.; Lee, Y. J.; Lee, K. C.; Lim, S. M.; Chi, D. Y.; Kim, K. M.; Park, J. A.; Choi, J. Y. Early Detection of A β Deposition in the 5xFAD Mouse by Amyloid PET. *Contrast Media Mol. Imaging* **2018**, *2018*. https://doi.org/10.1155/2018/5272014.

(76) Silva, I.; Silva, J.; Ferreira, R.; Trigo, D. Glymphatic System, AQP4, and Their Implications in Alzheimer's Disease. *Neurol. Res. Pract.* **2021**, *3* (1). https://doi.org/10.1186/s42466-021-00102-7.

(77) Quist, A.; Doudevski, I.; Lin, H.; Azimova, R.; Ng, D.; Frangione, B.; Kagan, B.; Ghiso, J.; Lal, R. Amyloid Ion Channels: A Common Structural Link for Protein-Misfolding Disease. *Proc. Natl. Acad. Sci. U. S. A.* **2005**, *102* (30), 10427–10432. https://doi.org/10.1073/pnas.0502066102.

(78) Elbert, D. L.; Patterson, B. W.; Lucey, B. P.; Benzinger, T. L. S.; Bateman, R. J. Importance of CSF-Based Aβ Clearance with Age in Humans Increases with Declining Efficacy of Blood-Brain Barrier/Proteolytic Pathways. *Commun. Biol.* **2022**, *5* (1), 1–13. https://doi.org/10.1038/s42003-022-03037-0.

(79) Xu, Z.; Xiao, N.; Chen, Y.; Huang, H.; Marshall, C.; Gao, J.; Cai, Z.; Wu, T.; Hu, G.; Xiao, M. Deletion of Aquaporin-4 in APP/PS1 Mice Exacerbates Brain Aβ Accumulation and Memory Deficits. *Mol. Neurodegener.* **2015**, *10* (1), 1–16. https://doi.org/10.1186/s13024-015-0056-1.

(80) Rosu, G. C.; Catalin, B.; Balseanu, T. A.; Laurentiu, M.; Claudiu, M.; Kumar-Singh, S.; Daniel, P. Inhibition of Aquaporin 4 Decreases Amyloid Aβ40 Drainage Around

Cerebral Vessels. *Mol. Neurobiol.* **2020**, *57* (11), 4720–4734. https://doi.org/10.1007/s12035-020-02044-8.

(81) Smith, A. J.; Verkman, A. S. The "Glymphatic" Mechanism for Solute Clearance in Alzheimer's Disease: Game Changer or Unproven Speculation? *FASEB J.* **2018**, *32* (2), 543–551. https://doi.org/10.1096/fj.201700999.

(82) Smith, A. J.; Duan, T.; Verkman, A. S. Aquaporin-4 Reduces Neuropathology in a Mouse Model of Alzheimer's Disease by Remodeling Peri-Plaque Astrocyte Structure. *Acta Neuropathol. Commun.* **2019**, *7* (1), 74. https://doi.org/10.1186/s40478-019-0728-0.

(83) Crescenzi, O.; Tomaselli, S.; Guerrini, R.; Salvadori, S.; D'Ursi, A. M.; Temussi, P. A.; Picone, D. Solution Structure of the Alzheimer Amyloid β-Peptide (1-42) in an Apolar Microenvironment: Similarity with a Virus Fusion Domain. *Eur. J. Biochem.* **2002**, *269* (22), 5642–5648. https://doi.org/10.1046/j.1432-1033.2002.03271.x.

(84) Fujimoto. 基因的改变NIH Public Access. *Bone* **2008**, *23* (1), 1–7. https://doi.org/10.1007/s11064-014-1374-3.Mechanisms.

(85) Ho, J. D.; Yeh, R.; Sandstrom, A.; Chorny, I.; Harries, W. E. C.; Robbins, R. A.; Miercke, L. J. W.; Stroud, R. M. Crystal Structure of Human Aquaporin 4 at 1.8 A and Its Mechanism of Conductance. *Proc. Natl. Acad. Sci. U. S. A.* **2009**, *106* (18), 7437–7442. https://doi.org/10.1073/pnas.0902725106.

(86) Lomize, M. A.; Pogozheva, I. D.; Joo, H.; Mosberg, H. I.; Lomize, A. L. OPM Database and PPM Web Server: Resources for Positioning of Proteins in Membranes. *Nucleic Acids Res.* **2012**, *40* (D1), 370–376. https://doi.org/10.1093/nar/gkr703.

(87) Allouche, A. Software News and Updates Gabedit — A Graphical User Interface for Computational Chemistry Softwares. *J. Comput. Chem.* **2012**, *32*, 174–182. https://doi.org/10.1002/jcc.

(88) Hess, B.; Kutzner, C.; Van Der Spoel, D.; Lindahl, E. GRGMACS 4: Algorithms for Highly Efficient, Load-Balanced, and Scalable Molecular Simulation. *J. Chem. Theory Comput.* **2008**, *4* (3), 435–447. https://doi.org/10.1021/ct700301q.

(89) Abraham, M. J.; Murtola, T.; Schulz, R.; Páll, S.; Smith, J. C.; Hess, B.; Lindah, E. Gromacs: High Performance Molecular Simulations through Multi-Level Parallelism from Laptops to Supercomputers. *SoftwareX* **2015**, *1–2*, 19–25. https://doi.org/10.1016/j.softx.2015.06.001.

(90) Mark, P.; Nilsson, L. Structure and Dynamics of the TIP3P, SPC, and SPC/E Water Models at 298 K. *J. Phys. Chem. A* **2001**, *105* (43), 9954–9960. https://doi.org/10.1021/jp003020w.

(91) Essmann, U.; Perera, L.; Berkowitz, M. L.; Darden, T.; Lee, H.; Pedersen, L. G. A Smooth Particle Mesh Ewald Method. *J. Chem. Phys.* **1995**, *103* (19), 8577–8593. https://doi.org/10.1063/1.470117.

(92) Hess, B.; Bekker, H.; Berendsen, H. J. C.; Fraaije, J. G. E. M. LINCS: A Linear Constraint Solver for Molecular Simulations. *J. Comput. Chem.* **1997**, *18* (12), 1463–1472. https://doi.org/10.1002/(SICI)1096-987X(199709)18:12<1463::AID-JCC4>3.0.CO;2-H.

(93) Zhu, F.; Tajkhorshid, E.; Schulten, K. Theory and Simulation of Water Permeation in Aquaporin-1. *Biophys. J.* **2004**, *86* (1 I), 50–57. https://doi.org/10.1016/S0006-3495(04)74082-5.

(94) Kumar, S.; Bouzida, D.; Swendsen, R. H.; Kollman, P. A.; Rosenberg, J. M. The Weighted Histogram Analysis Method for Free-Energy Calculations on Biomolecules. *J. Comput. Chem.* **1992**, *13* (8), 1011–1021.

(95) Qi, Y.; Ingólfsson, H. I.; Cheng, X.; Lee, J.; Marrink, S. J.; Im, W. CHARMM-GUI Martini Maker for Coarse-Grained Simulations with the Martini Force Field. *J. Chem. Theory Comput.* **2015**, *11* (9), 4486–4494. https://doi.org/10.1021/acs.jctc.5b00513.

(96) Marrink, S. J.; Risselada, H. J.; Yefimov, S.; Tieleman, D. P.; De Vries, A. H. The MARTINI Force Field: Coarse Grained Model for Biomolecular Simulations. *J. Phys. Chem. B* **2007**, *111* (27), 7812–7824. https://doi.org/10.1021/jp071097f.

(97) Yamada, Y.; Gohda, S.; Abe, K.; Togo, T.; Shimano, N.; Sasaki, T.; Tanaka, H.; Ono, H.; Ohba, T.; Kubo, S.; Ohkubo, T.; Sato, S. Carbon Materials with Controlled Edge Structures. *Carbon N. Y.* **2017**, *122* (October 1995), 694–701. https://doi.org/10.1016/j.carbon.2017.07.012.

(98) Maroli, N.; Bhasuran, B.; Natarajan, J.; Kolandaivel, P. The Potential Role of Procyanidin as a Therapeutic Agent against SARS-CoV-2: A Text Mining, Molecular Docking and Molecular Dynamics Simulation Approach. *J. Biomol. Struct. Dyn.* **2022**, *40* (3), 1230–1245. https://doi.org/10.1080/07391102.2020.1823887.

(99) Bastian, M.; Heymann, S.; Jacomy, M. Gephi: An Open Source Software for Exploring and Manipulating Networks Visualization and Exploration of Large Graphs. *Proc. Third Int. ICWSM Conf.* **2009**, 361–362.

Figures

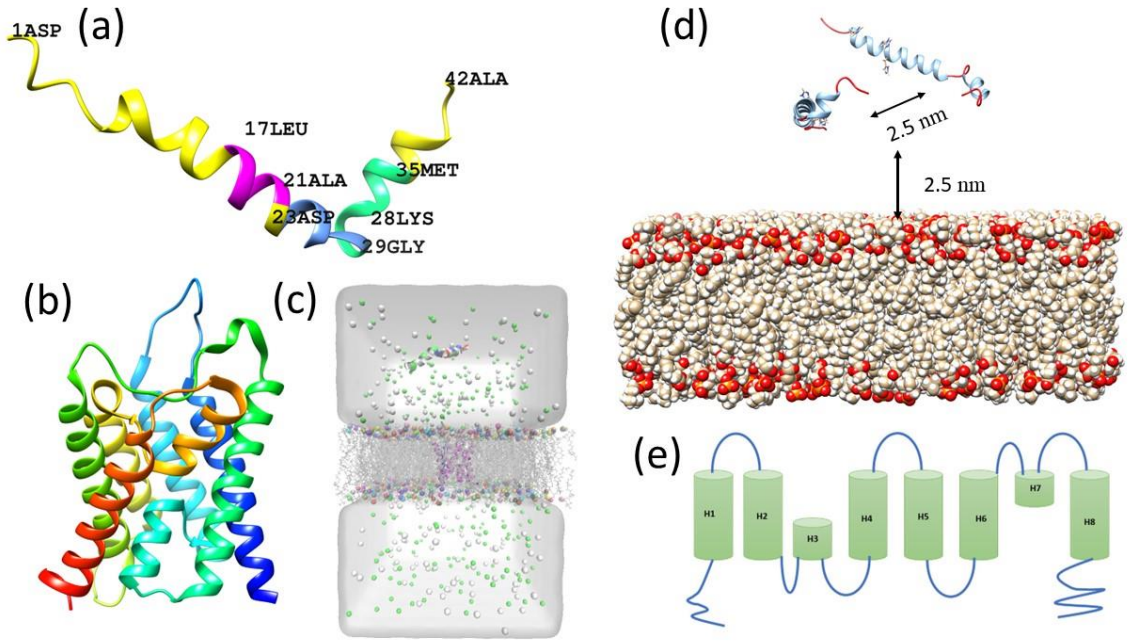

Figure 1. The simulation details: (a) represent the NMR structure of amyloid-β peptide. The central hydrophobic core region (Leu17-Ala21), loop region (Asp23-Lys28) and second hydrophobic region (Gly29-Met35) are presented in a different colour. (b) The X-ray crystal structure of the aquaporin-4 monomer unit and (c) represents the simulation system which comprises POPC lipid bilayer, water boxes, ions and aquaporin monomer units. (d) represents the initial position of amyloid dimer at the surface of the POPC lipid bilayer. The monomers are separated at a distance of 2.5 nm. (e) The representation of aquaporin monomer secondary structures. The helices are represented from H1-H8.

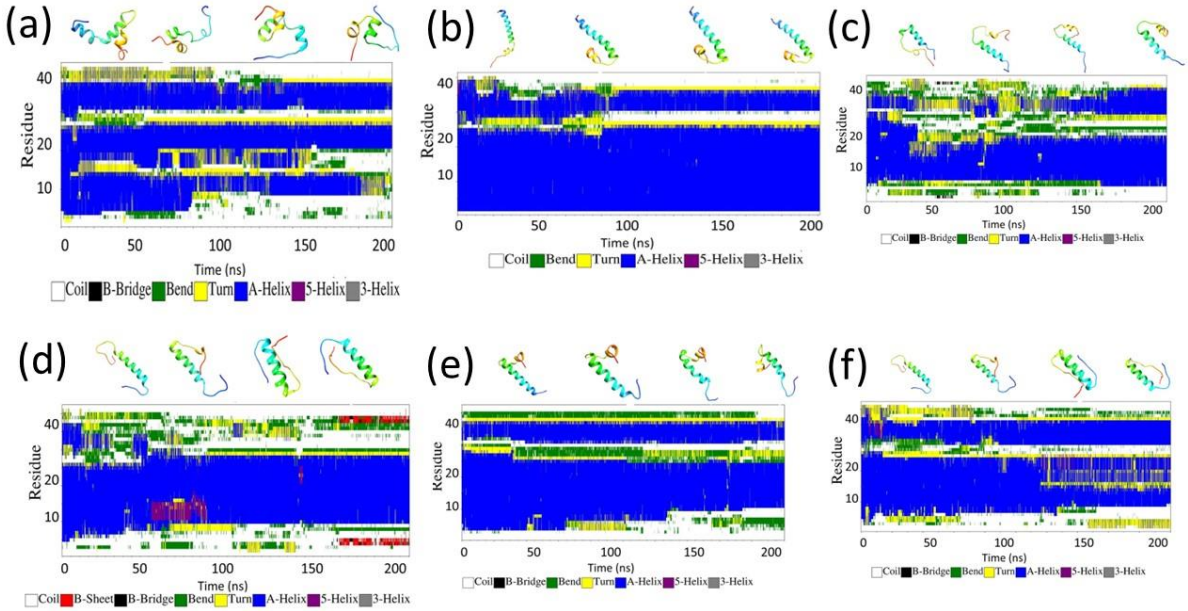

Figure 2. The time dependant secondary structural changes of the amyloid monomer and dimer at the surface of lipid and AQP4 channel. (a) represents the monomer at the surface of the POPC lipid bilayer showing the fast transformation from α-helix to coil structure. The presents of aquaporin-4 in the POPC membrane slow down the transition and retain the α-helix structure (b). The amyloid monomers of (c) and (d) dimer simulations show the transition of α-helix to coil and β-sheet formation. The presence of AQP4 retains the α-helix as represented in (e) and (f).

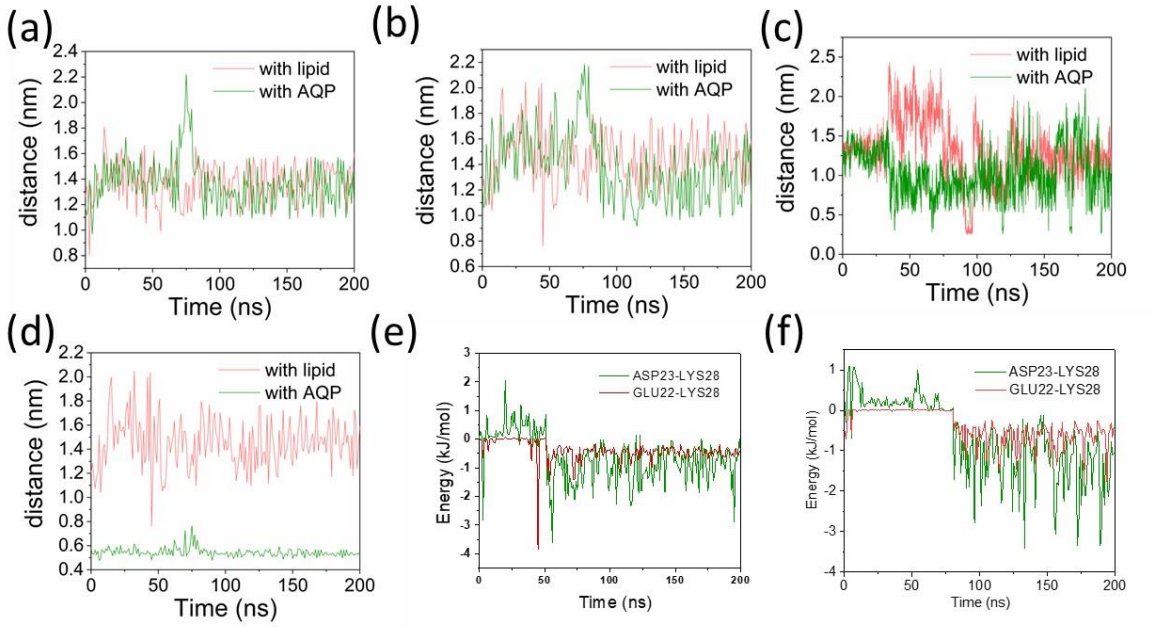

Figure 3. The salt bridge distances are calculated as the average distance between the CO^{2-} and NH^{3+} moiety of the residues. (a) represent the salt bridge distance between the residues Asp23-Lys28, (b) represent the salt bridge distance between Glu22-Lys28 and (c) represents the distance between the Val24-Asn27. The salt bridge distance between the amyloid monomer in the dimer lipid surface is represented in (d), there was only one salt bridge that appeared on one of the monomer units due to the strong interaction of peptide at the surface of the lipid bilayer. (e) and (d) represents the electrostatic interaction energy between the residues Asp23-Lys28 and Glu22-Lys28 at the surface of POPC and AQP4.

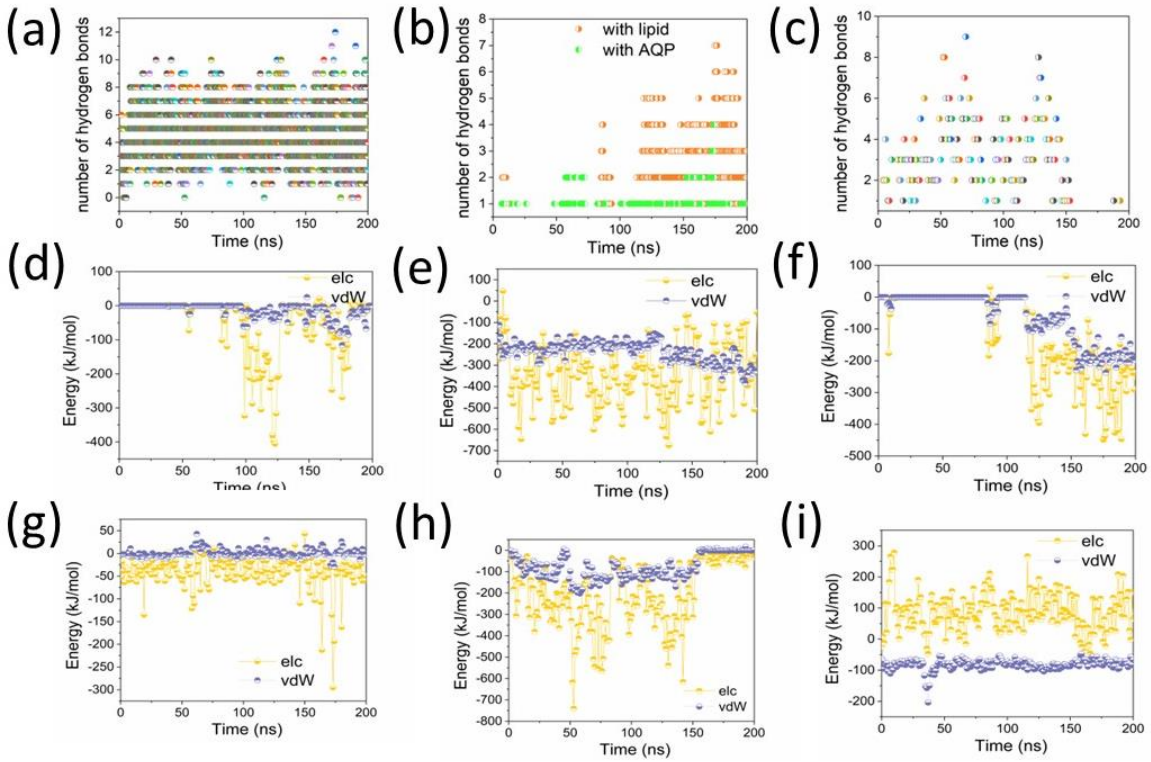

Figure 4. Hydrogen bond and non-bonded interaction energy analysis. (a) represents the number of hydrogen bonds between amyloid monomer and AQP4. (b) represents the number of hydrogen bonds between the peptides at the surface of the POPC and AQP4 channel and (c) represents the number of hydrogen bonds formed between the AQP4 channel and the whole dimer peptides. (d) and (e) represents the electrostatic and van der Waals interaction energy between the monomer and POPC lipid bilayer and AQP4, respectively. (f) and (g) represents the energy between the peptide at the surface of the POPC and AQP4 channel respectively. The individual peptide energy between peptides and AQP4 is represented in (h) and (i).

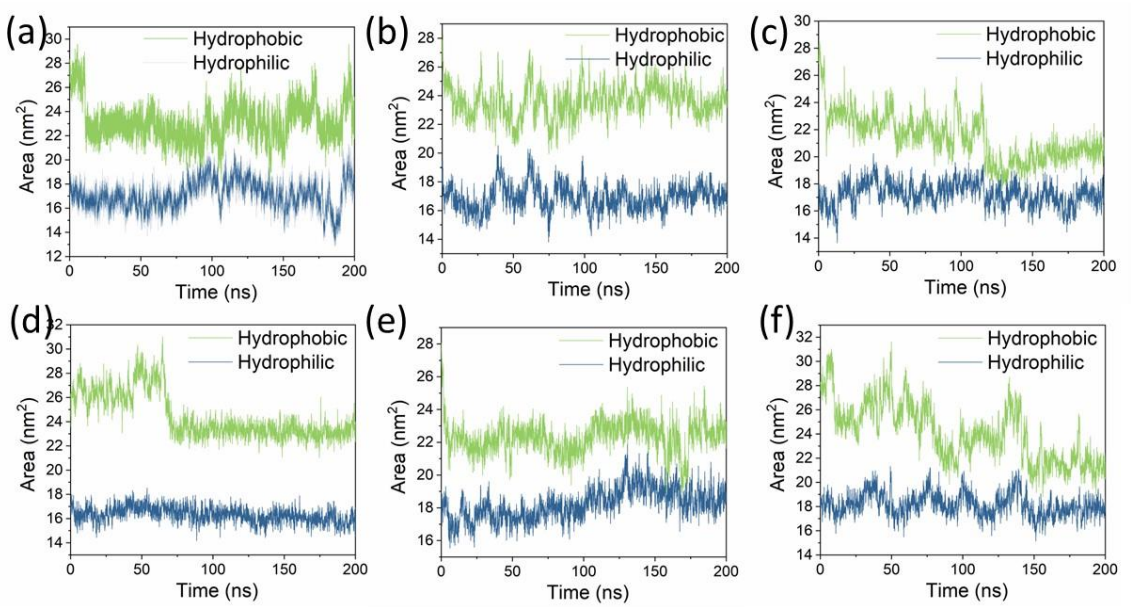

Figure 5. The hydrophobic and hydrophilic surface area of peptides. (a) represent the hydrophobic and hydrophilic area of amyloid monomer at the lipid surface and (b) represent the surface of AQP4. (c) and (e) represents the surface area of one of the monomers at the surface of POPC and AQP4 and (d) and (f) represent the surface area of the second monomer.

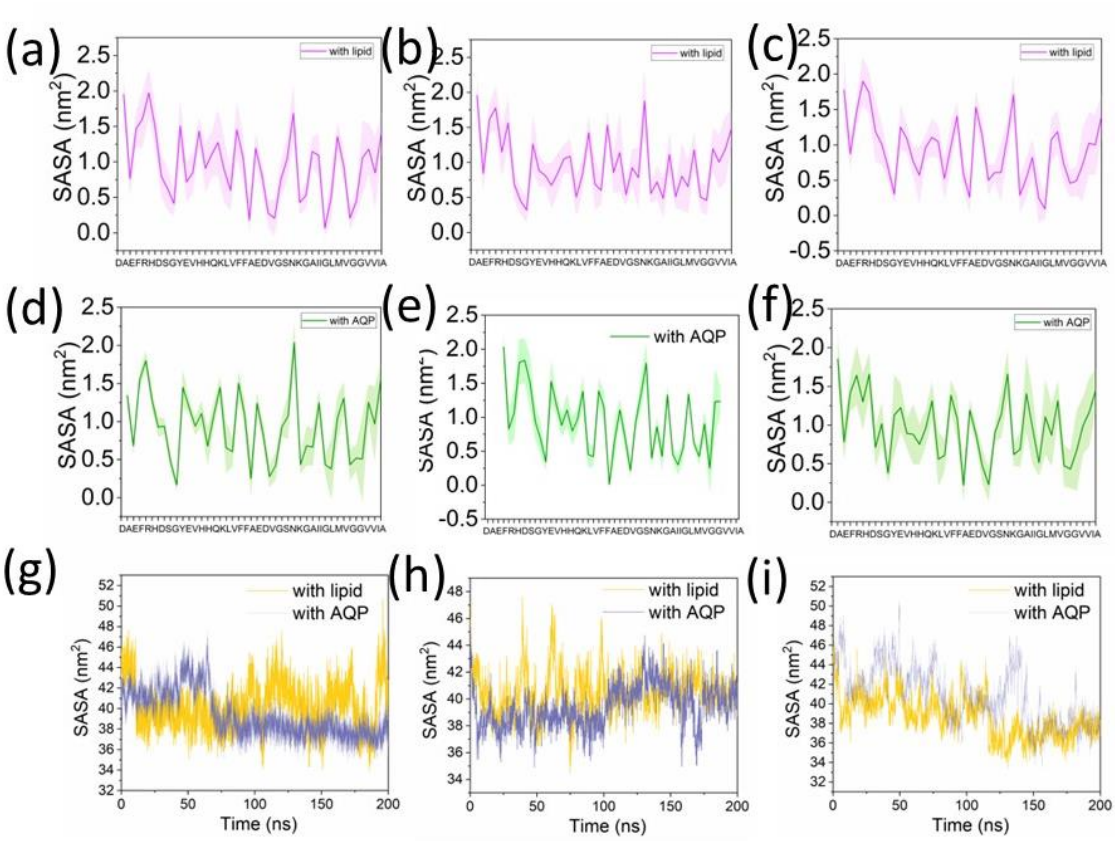

Figure 6. The individual residue solvent accessible surface area (SASA) of the peptide. (a)-(c) represents the residues SASA of monomers and monomers of the dimer on the surface of the POPC lipid bilayer. (d)-(f) represent the SASA of monomer and monomers of the dimer at the surface of the AQP4 channel. (g)-(i) represent the SASA with respect to time for the peptide at lipid and AQP4 surface.

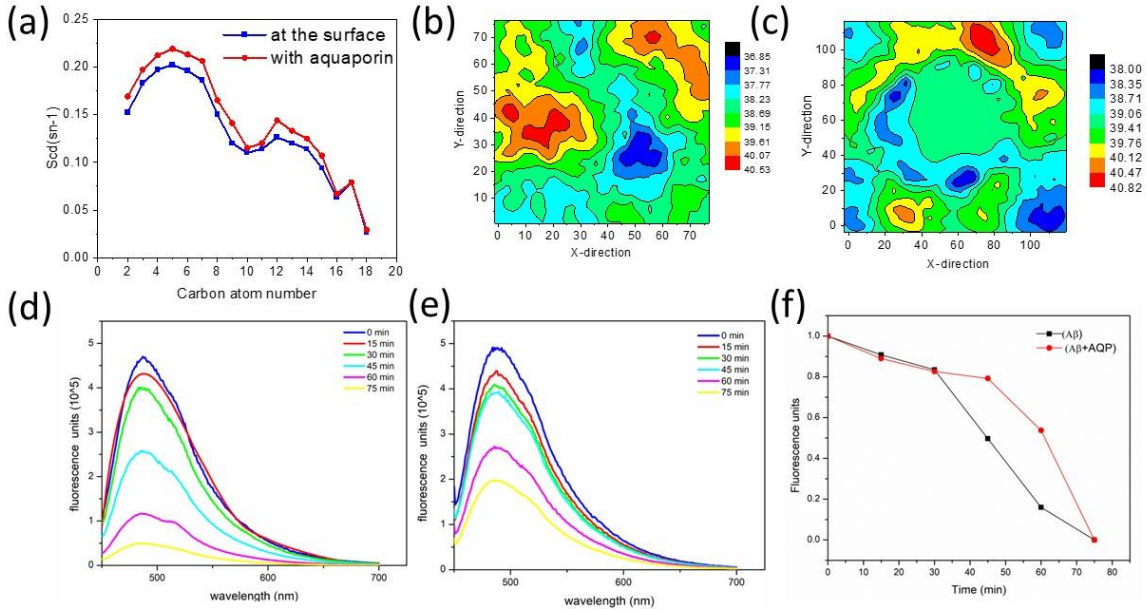

Figure 7. Aggregation of the peptides. (a) The lipid order parameter was calculated from 200 ns simulation for peptide at the surface. (b)and (c) represent the lipid thickness over 200 ns simulation time for monomers at the surface of POPC and AQP4. (d)-(f) represent the thioflavin T emission fluorescent spectra (range 450-700 nm) with excitation at 446 nm of the peptide and peptide without AQP4. (d) represent the aggregation based on the fluorescent intensity as the peak found to reduce over time indicates faster aggregation by losing the helical content. Whereas (e) represents the peptide with AQP4 and peaks found to reduce slowly over time, indicating slower aggregation. (f) represent the time-dependent aggregation of peptide, with AQP4 fluorescent intensity, is higher.

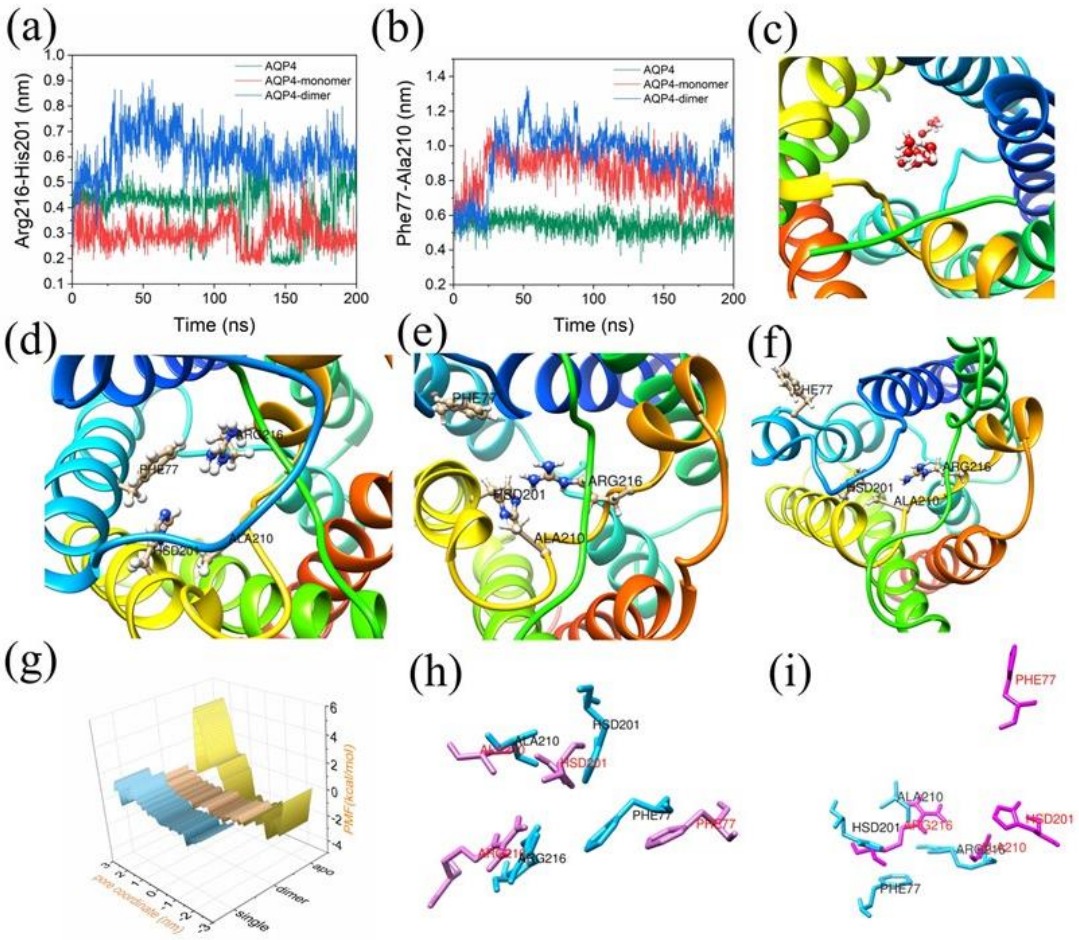

Figure 8. The dynamics of the AQP4 channel. (a) and (b) represent the distance between the residues at the pore region of the channel. These residues control the pore diameter, hence the selectivity of water molecules through the channel. The interaction of peptides is found to be affected by the inter-residue distances and results in the widening of the pore. (c) represent the vertical view of the normal single-line flow of the water molecules. (d) represent the vertical view of the residues Arg216, His201, Phe77 and Ala210 at the pore region for native AQP4 and (e) and (f) represent the same when interacting with the amyloid monomer and dimer. The energetics of water flow through the channel is calculated by obtaining the PMF profile (g), the native channel shows a high barrier at the selectivity filter which is found to be broken upon the interaction of monomer and dimer peptides. (h) and (i) represent the residue's alignment at the pore region while interacting with monomer and dimer peptides.

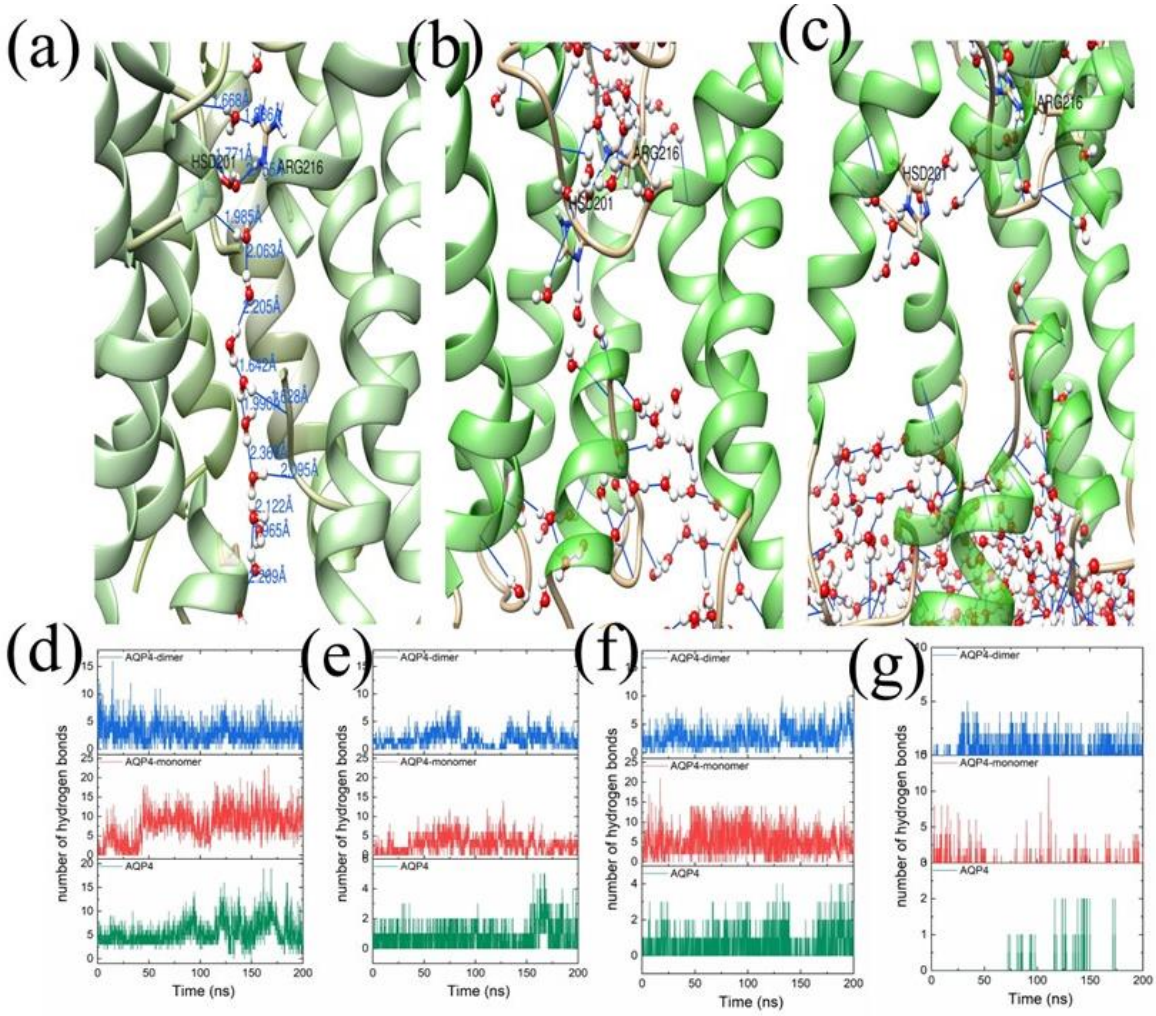

Figure 9. The single-line flow of the water is by creating and breaking the hydrogen bonds through the channel cavity. (a)-(c) represent the single line flow of the AQP4 channel, and disrupted water flow through the channel while interacting with amyloid monomer and dimer peptides respectively. (d)-(g) represent the number of hydrogen bonds that formed with water molecules and the residues Arg216, Ala210 His201 and Phe77 respectively.

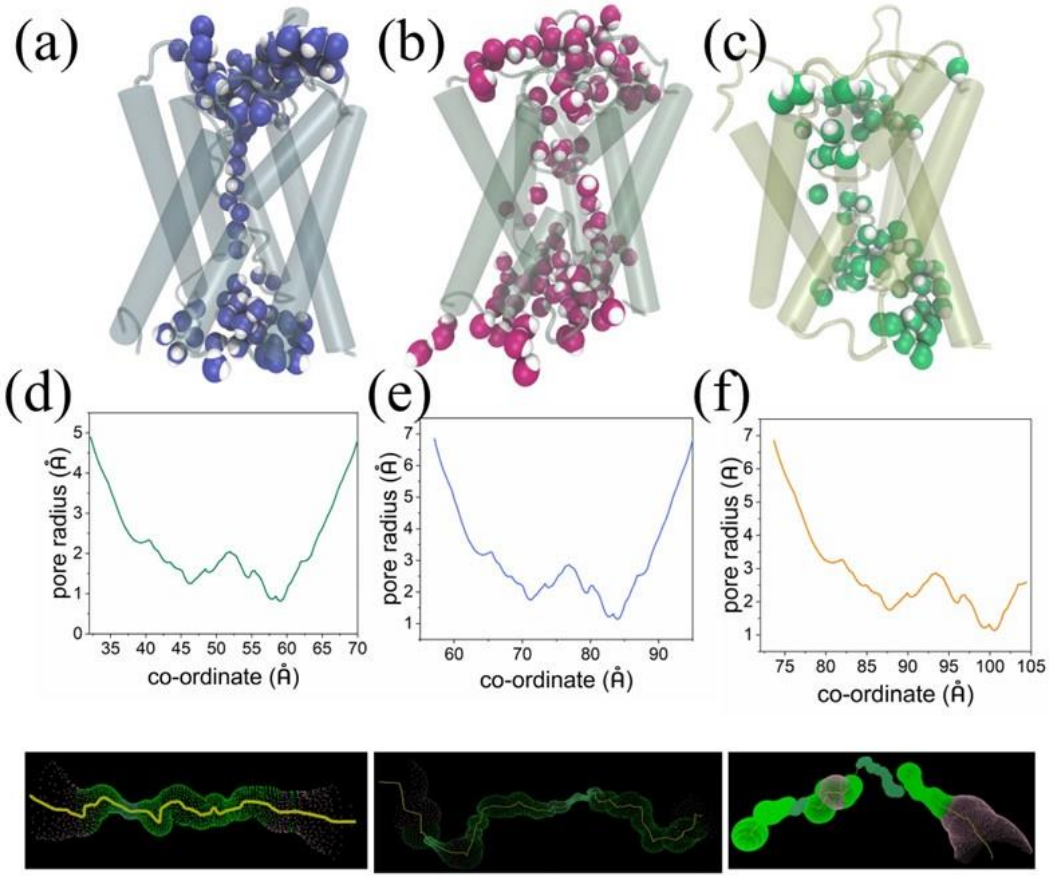

Figure 10. The single line flow of water and pore structure. (a) represent the native aquaporin-4 single-line water flow. (b) and (c) represent the disrupted water flow, the interaction of amyloid monomer (b) and dimer (c) led to bulk water flow through the channel. The pore diameter (d-f) also indicates the loss of selectivity filter in the channel.